doi.org/10.26434/chemrxiv.11663850.v1

Lewis Acid Coordination Redirects S-Nitrosothiol Reduction

Valiallah Hosseininasab, Alison C. McQuilken, Abolghasem (Gus) Bakhoda, Jeffery A. Bertke, Qadir K. Timerghazin, Timothy H. Warren

Submitted date: 20/01/2020 • Posted date: 22/01/2020

Citation information: Hosseininasab, Valiallah; McQuilken, Alison C.; Bakhoda, Abolghasem (Gus); Bertke, Jeffery A.; Timerghazin, Qadir K.; Warren, Timothy H. (2020): Lewis Acid Coordination Redirects S-Nitrosothiol Reduction. ChemRxiv. Preprint. https://doi.org/10.26434/chemrxiv.11663850.v1

S-Nitrosothiols (RSNOs) serve as air-stable reservoirs for nitric oxide in biology and are responsible for a myriad of physiological responses. While copper enzymes promote NO release from RSNOs by serving as Lewis acids capable of intramolecular electron-transfer, redox innocent Lewis acids separate these two functions to reveal the effect of coordination on structure and reactivity. The synthetic Lewis acid $B(C_6F_5)_3$ coordinates to the RSNO oxygen atom in adducts RSNO-$B(C_6F_5)_3$, leading to profound changes in the RSNO electronic structure and reactivity. Although RSNOs possess relatively negative reduction potentials (-1.0 to -1.1 vs. NHE), $B(C_6F_5)_3$ coordination increases their reduction potential by over 1 V into the physiologically accessible +0.1 V vs. NHE. Outer-sphere chemical reduction results in formation of the Lewis acid stabilized hyponitrite dianion trans-$[LA–O–N=N–O–LA]^{2-}$ (LA = $B(C_6F_5)_3$) that releases N_2O upon acidification. Mechanistic and computational studies support initial reduction to the $[RSNO\text{-}B(C_6F_5)_3]^{\bullet/-}$ radical-anion susceptible to N-N coupling prior to loss of RSSR.

File list (2)

MS-RSNO-Warren.pdf (1.28 MiB)	view on ChemRxiv • download file
SI-RSNO-Warren.pdf (7.66 MiB)	view on ChemRxiv • download file

Lewis Acid Coordination Redirects *S*-Nitrosothiol Reduction

Valiallah Hosseininasab,[a] Alison C. McQuilken,[a] Abolghasem (Gus) Bakhoda,[a] Jeffery A. Bertke,[a] Qadir K. Timerghazin,*[,b] and Timothy H. Warren*[,a]

[a]Department of Chemistry, Georgetown University, Box 571227-1227, Washington, D. C. 20057 United States

[b]Department of Chemistry, Marquette University, P.O. Box 1881, Milwaukee, WI 53201-1881, United States

Supporting Information Placeholder

ABSTRACT: *S*-Nitrosothiols (RSNOs) serve as air-stable reservoirs for nitric oxide in biology and are responsible for a myriad of physiological responses. While copper enzymes promote NO release from RSNOs by serving as Lewis acids capable of intramolecular electron-transfer, redox innocent Lewis acids separate these two functions to reveal the effect of coordination on structure and reactivity. The synthetic Lewis acid $B(C_6F_5)_3$ coordinates to the RSNO oxygen atom in adducts RSNO-$B(C_6F_5)_3$, leading to profound changes in the RSNO electronic structure and reactivity. Although RSNOs possess relatively negative reduction potentials (-1.0 to -1.1 vs. NHE), $B(C_6F_5)_3$ coordination increases their reduction potential by over 1 V into the physiologically accessible +0.1 V vs. NHE. Outer-sphere chemical reduction results in formation of the Lewis acid stabilized hyponitrite dianion *trans*-[LA–O–N=N–O–LA]$^{2-}$ (LA = $B(C_6F_5)_3$) that releases N_2O upon acidification. Mechanistic and computational studies support initial reduction to the [RSNO-$B(C_6F_5)_3$]$^{\bullet-}$ radical-anion susceptible to N-N coupling prior to loss of RSSR.

Nitric oxide (NO) is a key endogenous gasotransmitter which plays crucial signaling roles in vasorelaxation, neurotransmission and cytoprotection.[1] Nonetheless, NO has a short lifetime under biological conditions, under assault by omnipresent O_2 and $O_2^{\bullet-}$.[2] *S*-nitrosothiols (RSNOs) serve as air-stable NO reservoirs capable of facile NO release due to the modest RS–NO bond strength (~30 kcal mol^{-1}).[3-4] Circulating at near micromolar levels, RSNOs such as *S*-nitrosoglutathione serve as messengers themselves and participate in protein control via *S*-nitrosation of proteins, an important post-translational modification connected to health and disease.[5-7] For instance, *S*-nitrosation of hemoglobin at β-Cys93 is required for proper blood oxygenation.[8]

Redox active copper enzymes such as CuZn-SOD facilitate the release of NO from RSNOs.[9] Model studies revealed that Lewis acid coordination of RSNO to a copper(I) ion to form Cu^{I}-RSNO adducts precedes intramolecular electron transfer that releases NO. For instance, addition of the synthetic *S*-nitrosothiol Ph_3CSNO to the tris(pyrazolyl)borate complex ^{Mes}TpCu results in ^{Mes}TpCu^{I}(κ^1-N(O)SCPh$_3$) that reversibly loses NO with concomitant oxidation of the copper center to ^{Mes}TpCu^{II}-SCPh$_3$.[10] Given that the reduction potential of Ph_3CSNO (-1.25 V vs. NHE)[10] is dramatically more negative

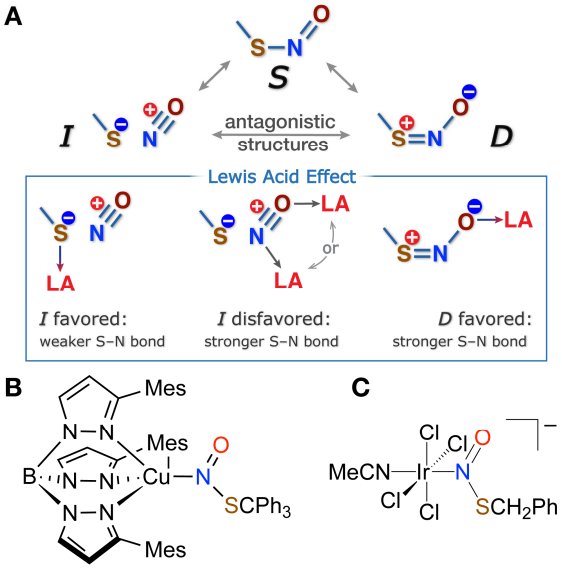

Figure 1. (**A**) Resonance representation of RSNO electronic structure and its modulation by Lewis acid coordination. (**B**) Known *N*-bound Lewis acid adducts of RSNOs.

than the corresponding [Cu^{II}]/[Cu^{I}] redox couple for a copper complex that releases NO with formation of the corresponding copper(II) thiolate [Cu^{II}]-SR (^{iPr2}TpCu(NCMe); $E_{1/2}$ = 270 mV vs. NHE),[11] coordination of the RSNO to the Lewis acid is clearly required to facilitate electron transfer.[10]

RSNOs exist in a variety of protein environments, exposed to a wide range of chemical stimuli including Lewis acids.[12-14] These stimuli can have a dramatic effect on the –SNO group properties owing to the unusual nature of the RSNO electronic structure, whose description requires a combination of the three resonance structures ***S***, ***D***, and ***I*** (Figure 1A). Two of these structures, ***D*** and ***I***, are *antagonistic*, i.e. have opposite bonding patterns and formal charges on atoms.[15] This antagonistic nature of RSNOs results in the paradoxical properties of the S–N bond, which exhibits restricted rotation suggestive of a partial double-bond character while being unusually long and weak,[16] as well as dual reactivity pattern of RSNO reactions.[15-17]

The antagonistic nature of RSNOs also suggests that Lewis acid coordination at N, S, or O atoms would radically alter the RSNO reactivity by favoring one antagonistic structure at the expense of the other (Figure 1A), an effect that may underline the enzymatic control of the RSNO reactions in bio-

logical environments.[15, 18-19] Due to the sensitive nature of RSNOs, experimental support for Lewis acid modulation of RSNO properties has lagged computational[16, 20-21] predictions. Seminal studies by Doctorovich revealed that *N*-coordination of RSNO to an Ir^{III} center in $[IrCl_4(NCMe)(\kappa^1\text{-}N(O)SR)]^-$ (R = CH_2Ph) to lead to shortening of the S–N bond, also seen in $^{Mes}TpCu^I(\kappa^1\text{-}N(O)SCPh_3)$.[22] While the S–N distance in Ph_3SNO is 1.792(5) Å,[23] $[IrCl_4(NCMe)(\kappa^1\text{-}N(O)SCH_2Ph)]^{-1}$ and $^{Mes}TpCu^I(\kappa^1\text{-}N(O)SCPh_3)$ possess S–N distances of 1.737(8) and 1.755(4) Å, each consistent with reduced ***I***- and increased ***D***-character of the κ^1-*N*-bound RSNO.

We experimentally find that *O*-coordination of a Lewis acid, however, has an even more profound effect on the RSNO reactivity due to the interaction with the oxygen atom which bears a formal negative charge in resonance structure ***D*** (Figure 1A). Addition of the oxophilic Lewis acid $B(C_6F_5)_3$ to synthetic RSNOs AdSNO (**1**) and $MesCH_2SNO$ (**2**) in pentane at RT leads to rapid color change from green to yellow for **1** or pink to orange for **2**. Crystallization from pentane provides Lewis acid adducts AdSNO-$B(C_6F_5)_3$ (**3**) and $MesCH_2SNO$-$B(C_6F_5)_3$ (**4**) in 80% and 71% yield, respectively (Figure 2). X-ray diffraction analysis confirms short S–N bonds in these adducts of 1.6252(17) and 1.608(5) Å in the *syn*- and *anti*-conformers of **3** and **4**, respectively. The observed dramatic contraction of the S–N bond is in agreement with DFT calculations at the ωB97XD-PCM(CH_2Cl_2)/ma-def2-TZVPP level (Figures S42-S44). At the same time, the experimental N–O bond lengths of 1.278(2) and 1.274(5) Å in **3** and **4** are longer than typical 1.18-1.19 Å N-O distances in free RSNOs.[23-25] These observations are consistent with increased contribution of the resonance component ***D*** in *O*-bound RSNO-$B(C_6F_5)_3$ complexes: indeed, calculations[26] suggest that the ***D*** weighting increases from ~30% in free RSNOs to ~55% in the $B(C_6F_5)_3$ adducts **3** and **4**.

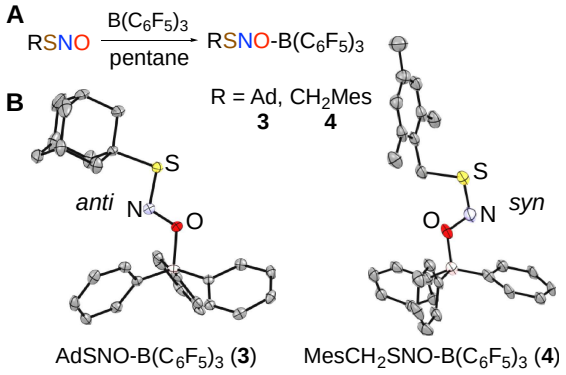

Figure 2. Synthesis (**A**) and X-ray structures (**B**) of AdSNO-$B(C_6F_5)_3$ (**3**) and $MesCH_2SNO$-$B(C_6F_5)_3$ (**4**); H and F atoms are not shown.

Dramatic structural alterations of RSNOs induced by *O*-coordination of a Lewis acid result in distinct spectroscopic changes. Consistent with trends revealed through X-ray structures, IR spectra report higher energy S–N stretches at 853 and 863 cm^{-1} for **3** and **4** relative to 645 and 630 cm^{-1} for the corresponding free RSNOs **1** and **2**. Conversely, the N–O stretching frequencies decrease to 1257 and 1282 for **3** and **4** relative to 1486 and 1484 cm^{-1} in **1** and **2**. Analysis of ^{15}N isotopomers of **1** - **4** confirms these assignments (Figures S5, S9, S16 and S23 in SI). As the oxygen atom lone pair becomes involved in dative bonding with $B(C_6F_5)_3$, the $n \rightarrow \pi^*$ adsorption characteristic to the UV-visible spectra of RSNOs shifts to higher energies. For instance, low intensity bands at 560 (5 M^{-1} cm^{-1}) and 600 nm (13 M^{-1} cm^{-1}) for AdSNO (**1**) shift to 510 nm (9 M^{-1} cm^{-1}) in AdSNO-$B(C_6F_5)_3$ (**3**), (Figures S4 and S15).

^{15}N NMR spectra of RSNOs typically reveal two signals for *anti*- and *syn*-conformers that require low temperature acquisition due to a relatively low barrier for S–N bond rotation ($\Delta G^{\ddagger}_{rot}$ = 10-14 kcal/mol).[23] For instance, the low temperature ^{15}N NMR spectrum of Ad$S^{15}NO$ in CD_2Cl_2 at -60 °C exhibits major and minor signal at δ 845.4 and 786.6 ppm (relative to NH_3), attributed to *anti* and *syn* conformers. Low temperature ^{15}N NMR spectra of crystallized adducts **3** and **4** dissolved in CD_2Cl_2 each exhibit three upfield shifted resonances. The major resonance for *O-anti*-AdSNO-$B(C_6F_5)_3$ (**3**) appears at δ 741 ppm, with two minor signals at 681 and 553 ppm. DFT calculations suggest that among the possible forms of AdSNO-$B(C_6F_5)_3$ the *O-syn* and *N-syn* species are closest in energy to the most stable *O-anti* form (enthalpies higher by 1.3 and 3.5 kcal/mol, Figures S43-S44), with predicted ^{15}N shifts at 755 and 605 ppm (compared to *O-anti* at 838 ppm). This allows us to tentatively assign the minor signals experimentally observed at δ 681 and 553 ppm to the *O-syn* and *N-syn* forms of **3**, respectively.

Besides the significant alteration of the RSNO geometry and spectral properties, Lewis acid coordination has a dramatic effect on the reduction potentials of RSNOs. Cyclic voltammograms (CVs) of free RSNOs **1** and **2** in CH_2Cl_2 each reveal two irreversible reduction features at rather negative potentials (Figures S24 and S28). The first corresponds to one-electron reduction of the free RSNO to the $[RSNO]^{\bullet-}$ radical-anion appearing at -1.13 and -1.01 V vs. NHE for **1** and **2**, respectively. The second peak in each at -1.32 V corresponds to the reduction of free NO released from reduced RSNO. Remarkably, AdSNO-$B(C_6F_5)_3$ (**3**) exhibits a quasi-reversible wave centered at +0.08 V vs. NHE, nearly 1 V higher than free AdSNO (**1**) that is also present under CV conditions (Figure 3). $MesCH_2SNO$-$B(C_6F_5)_3$ (**4**) also undergoes reduction at a potential ~1 V higher than free $MesCH_2SNO$ (**2**), but is largely irreversible under these conditions signaled by a reduction wave centered at +0.1 V vs. NHE (Figures S26 and S29).

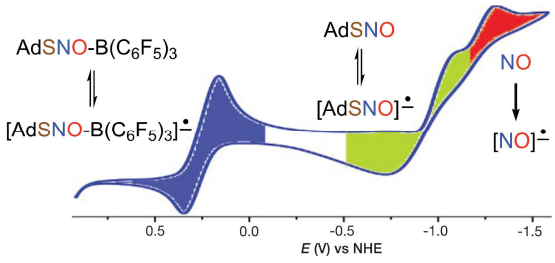

Figure 3. Cyclic voltammogram of AdSNO-$B(C_6F_5)_3$ (**3**) (7 mM) in CH_2Cl_2 at 25 °C with $[^nBu_4N][BPh_4]$ (0.1 M).

To provide greater insight into the species generated under CV conditions, we carried out chemical reduction with outer-sphere reductants. Addition of Cp^*_2Co (E_{red} = -1.24 V vs. NHE in CH_2Cl_2)[27] to free RSNOs **1** and **2** results in NO generation quantified in 82 and 71% yield, respectively (Figure 4A). This experimental finding is consistent with DFT calculations that suggest the $[RSNO]^{\bullet-}$ structure as a weakly bound complex of RS^- and $NO^{\bullet}$ (S–N distance >2.6 Å) with >95% of spin density on the NO moiety (Figure S45).

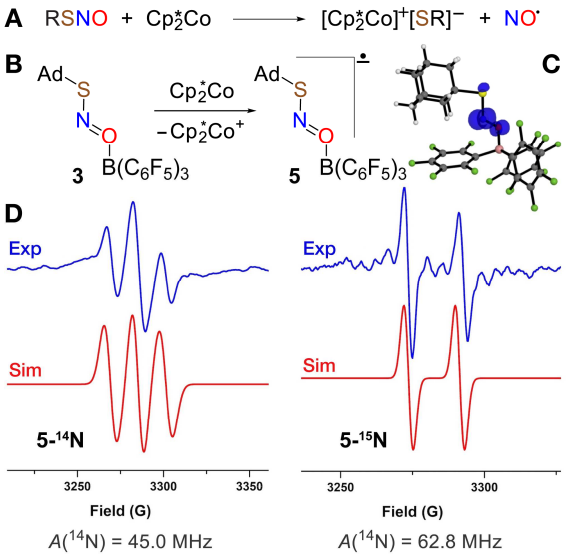

Figure 4. (**A**) Outer-sphere reduction of RSNO (R = Ad, $MesCH_2$) by Cp^*_2Co (**B**) Chemical reduction of AdSNO-$B(C_6F_5)_3$ by Cp^*_2Co. (**C**) Spin density plot of $[AdSNO\text{-}B(C_6F_5)_3]^{\bullet-}$ (**5**). (**D**) X-band EPR spectra of radical anions **5**-^{14}**N** and **5**-^{15}**N**.

The quasi-reversible reduction of AdSNO-$B(C_6F_5)_3$ (**3**) observed by cyclic voltammetry suggests that the radical anion $[AdSNO\text{-}B(C_6F_5)_3]^{\bullet-}$ (**5**) may have a long enough lifetime to enable characterization by EPR. Indeed, mixing a fluorobenzene solution of **3** with a pentane solution of Cp^*_2Co generates an intermediate with a three-line EPR signal at g = 1.999 (Figure 4D). This resonance is consistent with an *N*-centered radical anion predicted by DFT to exhibit extensive spin density on N (0.7 e^-, Figures 4C and S45B). The three-line pattern indicates strong coupling to the ^{14}N nucleus (I = 1; $A(^{14}N)$ = 45.0 MHz), confirmed via isotopic substitution with ^{15}N that gives a two line pattern (I = ½; $A(^{15}N)$ = 62.5 MHz) (Figure 4D). Attempts to observe $[MesCH_2SNO\text{-}B(C_6F_5)_3]^{\bullet-}$ by reduction of **4** with Cp^*_2Co under similar conditions did not allow for EPR observation of the corresponding radical anion consistent with its shorter lifetime indicated by the irreversible reduction peak in the CV of **4**.

Although DFT calculations predict elongated S–N and N–O bonds in $[AdSNO\text{-}B(C_6F_5)_3]^{\bullet-}$ (**5**) (1.71 Å and 1.33 Å; Figure S45) vs. AdSNO-$B(C_6F_5)_3$ (**3**) (1.61 Å and 1.25 Å), 1-electron reduction of AdSNO-$B(C_6F_5)_3$ does not seem to destabilize the S–N bond enough to encourage loss of NO$^\bullet$ as occurs in the reduction of free RSNOs (Figure 4A). Instead, reduction of Lewis acid adducts **3** and **4** ultimately delivers the Lewis acid stabilized hyponitrite dianion *trans*-$[(C_6F_5)_3BO\text{–}N{=}N\text{–}OB(C_6F_5)_3]^{2-}$ (**7**) (Figure 5). Addition of Cp^*_2Co to **3** or **4** gives dianion **7** charge-stabilized by 2 equiv. $Cp^*_2Co^+$ along with the corresponding disulfides AdS–SAd and $MesCH_2S\text{–}SCH_2Mes$ in 80 and 74% yield, respectively. Due to the mild reduction potentials of **3** and **4**, a range of metallocene reductants provide $[M]_2[(C_6F_5)_3BO\text{–}N{=}N\text{–}OB(C_6F_5)_3]$ (**7**-$[M]_2$; M = $Cp^*_2Co^+$, Cp_2Fe^+). The X-ray crystal structure of $[Cp^*_2Co^+]_2$ $[(C_6F_5)_3BO\text{–}N{=}N\text{–}OB(C_6F_5)_3]^{2-}$ (**7**-$[Cp^*_2Co^+]_2$) reveals N-N coupling to give a *trans* disposition of the $[O\text{–}N{=}N\text{–}O]^{2-}$ hyponitrite core located at a center of inversion with N–N' and O-N distances of 1.257(9) and 1.381(6) Å, respectively. These distances are similar to those found in other structures of the *trans*-hyponitrite anion.[28-29] ^{15}N NMR analysis of **7**-$[Cp^*_2Co^+]_2$ shows signals at δ 429.9 (major) and 384.9 (minor). We assign these as the *trans* and *cis* isomers of **7** based on DFT-predicted ^{15}N chemical shifts at δ 425 and 380 ppm, respectively. DFT also indicates a small difference of 1.6 kcal/mol in free energies for these isomers that favors the *trans* form (Figure S46).

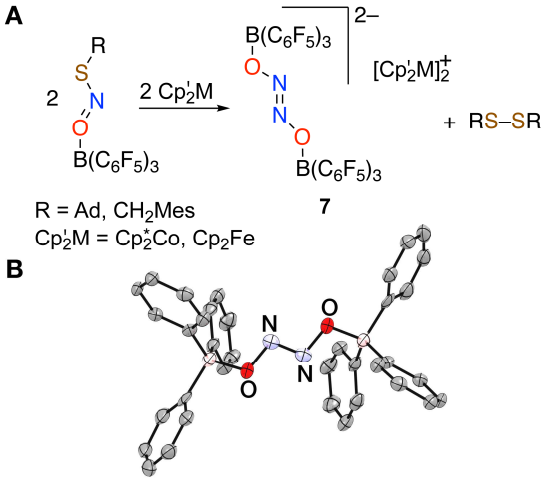

Figure 5. (**A**) Reduction RSNO-$B(C_6F_5)_3$ along with (**B**) the X-ray structure of the *trans*-hyponitrite dianion $[(C_6F_5)_3B\text{–}ON{=}NO\text{–}B(C_6F_5)_3]^{2-}$ (**7**); H and F atoms are not shown.

DFT calculations suggest that the radical anions $[RSNO\text{-}B(C_6F_5)_3]^{\bullet-}$ (R = Ad (**5**), $MesCH_2$ (**6**)) formed by 1-electron reduction of **3** and **4** undergo thermodynamically favorable dimerization via N–N bond formation to give dianions **8** and **9** (ΔG°_R = -6.5 and -6.7 kcal/mol, respectively). These dianions then lose the corresponding disulfide RS–SR (ΔG°_R = -39.0 and -41.3 kcal/mol, respectively) to give the doubly borane-capped hyponitrite dianion **7** (Figures 6 and S47-S48). Full reaction pathway calculations for a small model system (Figure S49) support the proposed mechanism with reasonably low barriers (<17 kcal/mol) for the dimer formation and the subsequent RS^- elimination, and a barrierless RS^- attack of to give disulfide RS–SR and Lewis acid capped hyponitrite.

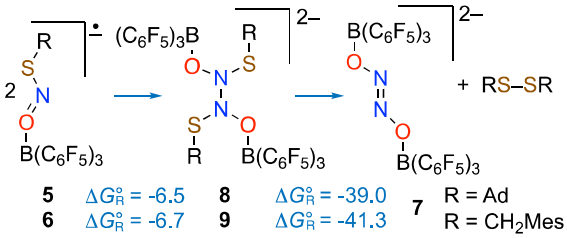

Figure 6. Stepwise conversion of $[RSNO\text{-}B(C_6F_5)_3]^{\bullet-}$ radical anions to dianion **7** and disulfide RS–SR. Reaction free energies (in kcal/mol at 298 K) calculated at the ωB97XD-PCM(CH_2Cl_2)/red-ma-def2-SV(P) level of theory.

Importantly, reaction of **7**-$[Cp^*_2Co^+]_2$ with 2 equiv. CF_3COOH triggers release of N_2O in 42-43% yield. Release of N_2O, the prototypical reactivity of hyponitrite upon protonation,[30] underscores how Lewis acids can redirect the chemical outcome of RSNO reduction which typically generates NO.

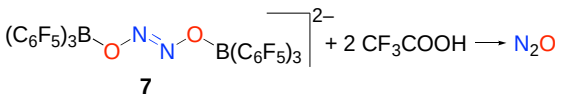

7

Figure 7. Reaction of (**7**-[Cp*$_2$Co]$_2$) with trifluoroacetic acid releases N_2O.

Lewis acid coordination via the O atom of *S*-nitrosothiols results in significant changes in the structure and chemical properties of the RSNO by strongly promoting its RS^+=N–O^- resonance component. Most profoundly, this mode of Lewis acid coordination redirects reduction of RSNOs to the hyponitrite dianion $[ON=NO]^{2-}$ rather than NO. Moreover, Lewis acid coordination significantly raises the reduction potential of RSNOs, enabling reduction by mild reductants. This represents a general strategy to facilitate reduction of small molecules, previously illustrated in the reduction of disulfides RSSR by ferrocene that only occurs in presence of a Lewis acid such as $B(C_6F_5)_3$.[31] Thus, Lewis acids could serve as a signaling motif to turn on outer sphere RSNO reduction in the vicinity of electron-transfer proteins that function in the range of +700 to -800 mV vs. NHE.[32] Future studies will examine connection between Lewis acid strength and reduction potential, including Lewis acids that serve as H-bond donors that could directly promote N_2O formation.

ASSOCIATED CONTENT

Supporting Information. This material is available free of charge via the Internet at http://pubs.acs.org. Experimental, characterization, and computational details (PDF), X-ray crystallographic data of **3**, **4**, **7**-[Cp*$_2$Co$^+$]$_2$ and **7**-[Cp$_2$Fe]$_2$ (CIF), XYZ coordinates of calculated structures.

AUTHOR INFORMATION

Corresponding Authors

thw@georgetown.edu (T.H.W.);
qadir.timerghazin@marquette.edu (Q.K.T.)

Notes

The authors declare no competing financial interest.

ACKNOWLEDGMENT

T.H.W. acknowledges the NIH (R01GM126205) and the Georgetown Environment Initiative. Q.K.T. acknowledges NSF CAREER award CHE–1255641, and Marquette University Way-Klinger Sabbatical Award. V.H. thanks Mahdi Raghibi Boroujeni and Dr. Pokhraj Ghosh for assistance with CV experiments. This work used the high-performance computing cluster at the Extreme Science and Engineering Discovery Environment (XSEDE) supported by NSF grant ACI-1053575.

REFERENCES

(1) Ignarro, L., *Nitric Oxide Biology and Pathobiology*. 2nd ed. 2009, p 845.
(2) Rassaf, T.; Kleinbongard, P.; Preik, M.; Dejam, A.; Gharini, P.; Lauer, T.; Erckenbrecht, J.; Duschin, A.; Schulz, R.; Heusch, G.; Feelisch, M.; Kelm, M., Plasma nitrosothiols contribute to the systemic vasodilator effects of intravenously applied NO Experimental and clinical study on the fate of NO in human blood. *Circ. Res.* **2002,** *91*, 470-477.
(3) Smith, B. C.; Marletta, M. A., Mechanisms of S-nitrosothiol formation and selectivity in nitric oxide signaling. *Curr Opin Chem Biol* **2012,** *16*, 498-506.
(4) Bartberger, M. D.; Mannion, J. D.; Powell, S. C.; Stamler, J. S.; Houk, K. N.; Toone, E. J., S–N Dissociation Energies of S-Nitrosothiols: On the Origins of Nitrosothiol Decomposition Rates. *J. Am. Chem. Soc.* **2001,** *123* (36), 8868-8869.
(5) Nakamura, T.; Tu, S.; Akhtar, M. W.; Sunico, C. R.; Okamoto, S. I.; Lipton, S. A., Aberrant protein S-nitrosylation in neurodegenerative diseases. *Neuron* **2013,** *78* (4), 596-614.
(6) McMahon, T. J.; Ahearn, G. S.; Moya, M. P.; Gow, A. J.; Huang, Y. C.; Luchsinger, B. P.; Nudelman, R.; Yan, Y.; Krichman, A. D.; Bashore, T. M.; Califf, R. M.; Singel, D. J.; Piantadosi, C. A.; Tapson, V. F.; Stamler, J. S., A nitric oxide processing defect of red blood cells created by hypoxia: deficiency of *S*-nitrosohemoglobin in pulmonary hypertension *Proc. Natl Acad. Sci. USA* **2005,** *102*, 14801-14806.
(7) Hess, D. T.; Matsumoto, A.; Kim, S. O.; Marshall, H. E.; Stamler, J. S., Protein *S*-nitrosylation: purview and parameters. *Nature Rev. Mol. Cell Biol.* **2005,** *6*, 150-166.
(8) Allen, B. W.; Stamler, J. S.; Piantadosi, C. A., Hemoglobin, nitric oxide and molecular mechanisms of hypoxic vasodilation. *Trends Mol Med* **2009,** *15*, 452-460.
(9) Johnson, M. A.; Macdonald, T. L.; Mannick, J. B.; Conaway, M. R.; Gaston, B., Accelerated *S*-nitrosothiol breakdown by amyotrophic lateral sclerosis mutant copper, zinc-superoxide dismutase *J. Biol. Chem.* **2011,** *276*, 39872-39878.
(10) Zhang, S.; Melzer, M. M.; Nermin, S. S.; Çelebi-Ölçüm, N.; Warren, T. H., A motif for reversible nitric oxide interactions in metalloenzymes. *Nat. Chem.* **2016,** *8*, 663-669.
(11) Fujisawa, K.; Ono, T.; Ishikawa, Y.; Amir, N.; Miyashita, Y.; Okamoto, K.; Lehnert, N., Structural and Electronic Differences of Copper(I) Complexes with Tris(pyrazolyl)methane and Hydrotris(pyrazolyl)borate Ligands. *Inorg. Chem.* **2006,** *45*, 1698-1713.
(12) Stomberski, C. T.; Hess, D. T.; Stamler, J. S., Protein S-Nitrosylation: Determinants of Specificity and Enzymatic Regulation of S-Nitrosothiol-Based Signaling. *Antioxid. Redox Signal.* **2019,** *30*, 1331-1351.
(13) Seth, D.; Hess, D. T.; Hausladen, A.; Wang, L.; Wang, Y.-J.; Stamler, J. S., A Multiplex Enzymatic Machinery for Cellular Protein S-nitrosylation. *Molecular Cell* **2018,** *69* (3), 1-21.
(14) Anand, P.; Stamler, J. S., Enzymatic mechanisms regulating protein S-nitrosylation: implications in health and disease. *J. Mol. Med.* **2012,** *90*, 233-244.
(15) Talipov, M. R.; Timerghazin, Q. K., Protein Control of *S*-Nitrosothiol Reactivity: Interplay of Antagonistic Resonance Structures. *J. Phys. Chem. B* **2013,** *117*, 1827–1837.
(16) Timerghazin, Q. K.; Peslherbe, G. H.; English, A. M., Resonance Description of *S*-Nitrosothiols: Insights into Reactivity. *Org. Lett.* **2007,** *9*, 3049-3052.
(17) Ivanova, L. V.; Cibich, D.; Deye, G.; Talipov, M. R.; Timerghazin, Q. K., Modeling of S-Nitrosothiol-Thiol Reactions of Biological Significance: HNO Production by S-Thiolation Requires a Proton Shuttle and Stabilization of Polar Intermediates. *Chem. Bio. Chem* **2017,** *18*, 726-738.
(18) Moran, E. E.; Timerghazin, Q. K.; Kwong, E.; English, A. M., Kinetics and Mechanism of *S*-Nitrosothiol Acid-Catalyzed Hydrolysis: Sulfur Activation Promotes Facile NO^+ Release. *J. Phys. Chem. B* **2011,** *115*, 3112–3126.
(19) Timerghazin, Q. K.; Talipov, M. R., Unprecedented External Electric Field Effects on *S*-Nitrosothiols: Possible Mechanism of Biological Regulation? . *J. Phys. Chem. Lett.* **2013,** *4*, 1034–1038.
(20) Baciu, C.; Cho, K.-B.; Gauld, J. W., Influence of Cu^+ on the RS–NO Bond Dissociation Energy of *S*-Nitrosothiols. *J. Phys. Chem. B* **2005,** *109* (4), 1334-1336.
(21) Talipov, M. R.; Khomyakov, D. G.; Xian, M.; Timerghazin, Q. K., Computational design of *S*-nitrosothiol "click" reactions. *J. Comp. Chem.* **2013,** *34* (18), 1527-1530.
(22) Perissinotti, L. L.; Estrin, D. A.; Leitus, G.; Doctorovich, F., A surprisingly stable *S*-nitrosothiol complex *J. Am. Chem. Soc.* **2006,** *128*, 2512-2513.
(23) Arulsamy, N.; Bohle, D. S.; Butt, J. A.; Irvine, G. J.; Jordan, P. A.; Sagan, E., Interrelationships between conformational dynamics and the redox chemistry of *S*-nitrosothiols. *J. Am. Chem. Soc.* **1999,** *121*, 7115-7123.

(24) Goto, K.; Hino, Y.; Kawashima, T.; Kaminaga, M.; Yano, E.; Yamamoto, G.; Takagi, N.; Nagase, S., Synthesis and crystal structure of a stable S-nitrosothiol bearing a novel steric protection group and of the corresponding S-nitrothiol. *Tetrahedron Lett* **2000,** *41*, 8479-8483.
(25) Spivey, A. C.; Colley, J.; Sprigens, L.; Hancock, S. M.; Cameron, D. S.; Chigboh, K. I.; Veitch, G.; Frampton, C. S.; Adams, H., The synthesis of water soluble decalin-based thiols and S-nitrosothiols—model systems for studying the reactions of nitric oxide with proteinthiols. *Org. Biomol. Chem.* **2005,** *3*, 1942-1952.
(26) Glendening, E. D.; Landis, C. R.; Weinhold, F., Resonance Theory Reboot. *J. Am. Chem. Soc.* **2019,** *141* (10), 4156-4166.
(27) Connelly, N. G.; Geiger, W. E., Chemical Redox Agents for Organometallic Chemistry. *Chem. Rev.* **1996,** *96*, 877-910.
(28) Chen, L. H.; Laan, J., Vibrational Spectra and Force Constants for trans-Sodium Hyponitrite. *J. Raman Spectrosc.* **1983,** *14*, 284-287.
(29) Wijeratne, G. B.; Hematian, S.; M A Siegler; Karlin, K. D., Copper(I)/$NO_{(g)}$ Reductive Coupling Producing a trans-Hyponitrite Bridged Dicopper(II) Complex: Redox Reversal Giving Copper(I)/NO(g) Disproportionation. *J. Am. Chem. Soc.* **2017,** *139*, 13276–13279.
(30) Wright, A. M.; Hayton, T. W., Understanding the Role of Hyponitrite in Nitric Oxide Reduction *Inorg. Chem.* **2015,** *54*, 9330-9341.
(31) Liu, L. L.; Cao, L. L.; Shao, Y.; Stephan, D. W., Single Electron Delivery to Lewis Pairs: An Avenue to Anions by Small Molecule Activation. *J. Am. Chem. Soc.* **2017,** *139*, 10062–10071.
(32) Liu, J.; Chakraborty, S.; Hosseinzadeh, P.; Yu, Y.; Tian, S.; Petrik, I.; Bhagi, A.; Lu, Y., Metalloproteins Containing Cytochrome, Iron–Sulfur, or Copper Redox Centers. *Chem. Rev.* **2014,** *114*, 4366-4469.

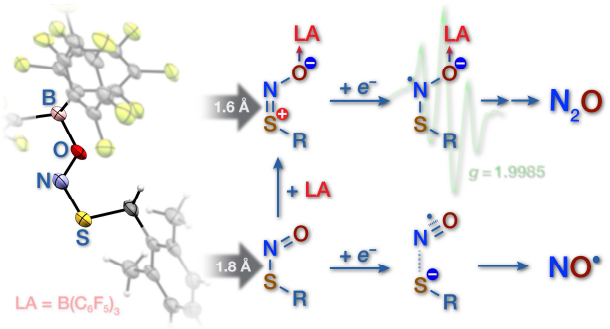
B
O
N
S
LA = B(C6F5)3
1.6 Å
1.8 Å
LA
N
O
S
R
+ e⁻
+ LA
N2O
NO•
g = 1.9985

Supplementary Material for:

Lewis Acid Coordination Redirects *S*-Nitrosothiol Reduction

Valiallah Hosseininasab,[a] Alison C. McQuilken,[a] Abolghasem (Gus) Bakhoda,[a] Jeffery A. Bertke,[a] Qadir Timerghazin,[b,*] and Timothy H. Warren[a,*]

[a]Department of Chemistry, Georgetown University, Box 571227, Washington, DC 20057-1227, USA

[b]Department of Chemistry, Marquette University, P.O. Box 1881, Milwaukee, Wisconsin 53201-1881, United States

Corresponding authors email:

qadir.timerghazin@marquette.edu (Q.T.)
thw@georgetown.edu (T.H.W.)

Table of Contents

1. General Instrumentation and Physical Methods

All experiments were carried out under dry nitrogen atmosphere by utilizing MBraun gloveboxes and/or standard Schlenk techniques unless otherwise mentioned. ^{1}H and ^{19}F NMR and $^{13}C\{^{1}H\}$ NMR spectra were recorded on a Varian 400 MHz spectrometer at room temperature unless otherwise noted. Variable temperature ^{15}N NMR experiments were recorded on a Varian 400 MHz spectrometer at -70 °C to 20 °C range. The chemical shift (δ) values are expressed in ppm relative to tetramethylsilane, whereas the residual ^{1}H signal of deuterated solvent served as an internal standard. Elemental analyses were performed on a Perkin-Elmer PE2400 micro-analyzer at Georgetown University. UV-vis spectra were recorded on Agilent 8454 Diode Array spectrometer equipped with stirrer and Unisoku USP-203 cryostat. The molar extinction coefficients of different isolated complexes were determined from Beer's law plots (absorbance *vs* concentration) with at least four different concentrations. IR spectra (with spectral resolution of 2 cm^{-1}) were collected on an ATR spectrometer. Details for X-ray crystallography appear in Section 15.

2. Materials

All chemicals were purchased from common vendors (e.g. Sigma-Aldrich, Acros Organics, Strem Chemicals, TCI) and used without further purification unless otherwise mentioned. $MesCH_2SH$ and Tetrabutylammonium tetraphenylborate ($[NBu_4][BPh_4]$ were obtained from Sigma-Aldrich and tris(pentafluorophenyl)borane was obtained from Boulder Scientific Company and used without further purification. Molecular sieves (4A, 4-8 mesh beads) were obtained from Fisher Scientific and were activated prior to use in vacuo at 200 °C for 24 h. Extra dry solvents (≥99.5%) with Acroseal® and deuterated solvents were purchased from Acros Organics and Cambridge Isotope Laboratories, respectively. Both anhydrous and deuterated solvents were sparged with nitrogen and stored over activated 4A molecular sieves under a nitrogen atmosphere. Nitric oxide gas (unlabeled) was obtained from Praxair and purified by passing through a column of Ascarite (8-20 mesh) purchased from Sigma.

3. Synthesis and Characterization of AdSNO (1)

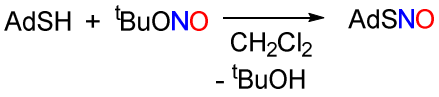

Scheme S1. Synthesis of AdSNO (**1**).

The synthesis of AdSNO has been previously reported,[1] but we include full characterization data here to allow for careful comparison between AdSNO and its tris(pentafluorophenyl)borane adduct AdSNO-B(C_6F_5)$_3$.

^{t}BuONO (1.225 g, 11.883 mmol) was directly added to a solution of AdSH (0.5 g, 2.97 mmol) in dichloromethane (*ca.* 3 mL). The solution was stirred for 0.5 h at RT and the resultant dark green solution was dried to obtain a dark green solid (0.530 g, 2.686 mmol) in 90% yield.

Ad$S^{15}NO$ was prepared analogously from ^{t}Bu$O^{15}NO$.[2]

^{1}H NMR (400 MHz, 298 K, $CDCl_3$): δ 2.54 (d, 6H, CH_2), 2.29 (t, 3H, C*H*), 1.93 (d, 6H, CH_2) (Figure S1);

$^{13}C\{^1H\}$ NMR (100 MHz, 298 K, $CDCl_3$): δ 55.77, 43.60, 36.38, 30.11.

^{15}N NMR (41 MHz, 20 °C, CD_2Cl_2): δ 839.60 (s, Ad$S^{15}NO$) (Figure S2).

^{15}N NMR (41 MHz, -70 °C, CD_2Cl_2): δ 845.35 (s, *anti*, Ad$S^{15}NO$), δ 786.56 (s, *syn*, Ad$S^{15}NO$) (Figure S3).

UV-Vis (CH_2Cl_2, 25 °C): λ_{max}/nm (ε/$M^{-1}cm^{-1}$) = 561 (5), 601 (13) (Figure S4).

FT-IR (cm^{-1}): 1486 $\nu(^{14}NO)$; 645 $\nu(S\text{-}^{14}N)$; 1455 $\nu(^{15}NO)$; 629 $\nu(S\text{-}^{15}N)$; Hooke's law predicts $^{15N/14N}\Delta\nu$ = 27 cm^{-1} and $^{15N/14N}\Delta\nu$ = 15, respectively (Figure S5). The IR spectra were taken by putting AdSNO as a fine powder directly on the ATR instrument.

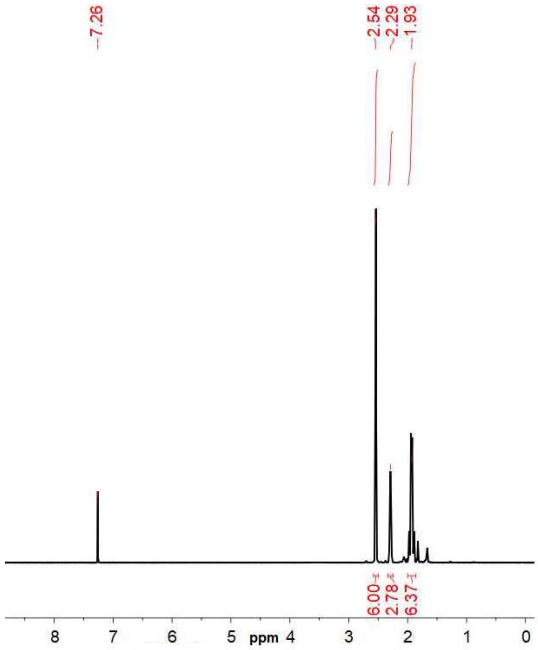

Figure S1. ^{1}H NMR spectrum (400 MHz, 25 °C, $CDCl_3$) of AdSNO (**1**).

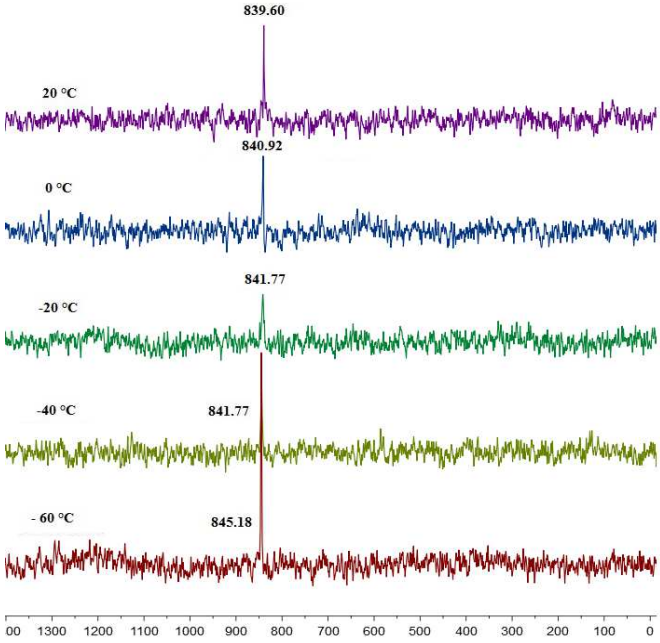

Figure S2. Variable temperature ^{15}N NMR spectra (41 MHz, CD_2Cl_2) of AdS^{15}NO (**1**-^{15}**N**).

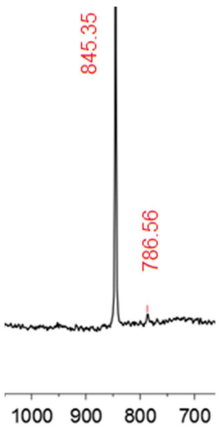

Figure S3. ^{15}N NMR spectrum (41 MHz, CD_2Cl_2) of AdS^{15}NO (**1**-^{15}**N**) at -70 °C.

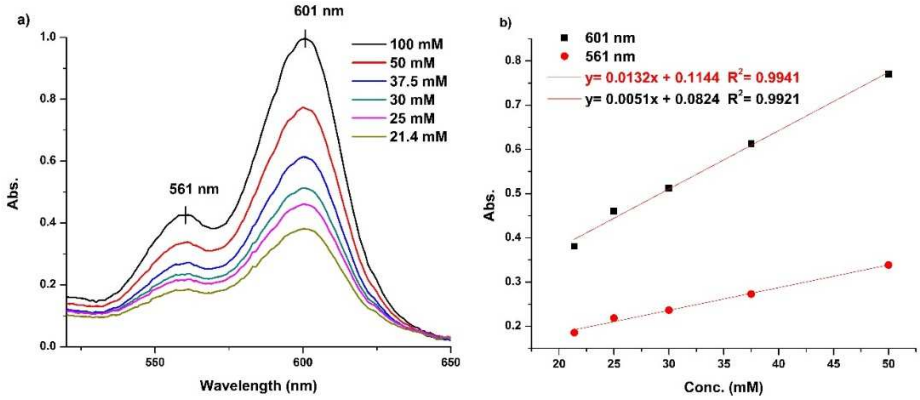

Figure S4. (a) UV-Vis spectra of AdSNO (**1**) in dichloromethane at 25 °C at different concentrations. (b) Beer's law plot for (**1**) depicts λ_{max} = 561 nm (ε = 5 $M^{-1}cm^{-1}$) and λ_{max} = 601 nm (ε = 13 $M^{-1}cm^{-1}$)

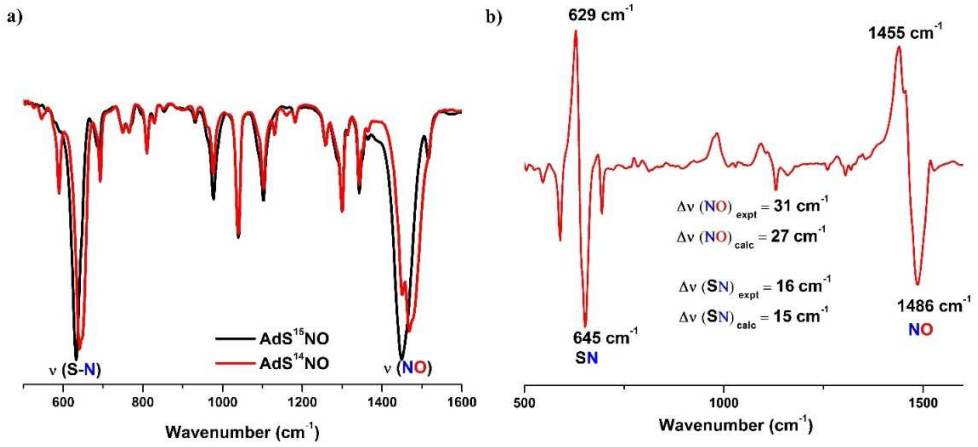

Figure S5. a) FT-IR spectra of AdS^{14}NO (**1**) (red trace) and AdS^{15}NO (**1**-^{15}**N**) (black trace). b) The difference spectrum between (**1**) (down) and (**1**-^{15}**N**) (up).

4. Synthesis and Characterization of $MesCH_2SNO$ (2)

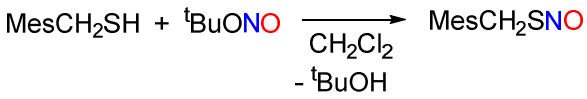

Scheme S2. Synthesis of $MesCH_2SNO$.

^{t}BuONO (0.744 g, 7.216 mmol) was directly added to a solution of $MesCH_2SH$ (0.3 g, 1.804 mmol) in dichloromethane at -40 °C (*ca.* 3 mL). The solution was stirred for 10 min at RT and the resultant dark pink solution was dried to obtain dark pink oil (0.31 g, 1.587 mmol) in 88% yield.

^{1}H NMR (400 MHz, 298 K, $CDCl_3$): δ 6.83 (s, 2H, Aryl-CH), 4.70 (s, 2H, C*H*$_2$), 2.25 (s, 3H, CH_3), 2.16 (s, 6H, CH_3) (Figure S6).

^{13}C{^{1}H} NMR (100 MHz, 298 K, $CDCl_3$): *δ* 137.36, 137.03, 129.28, 129.22, 32.15, 20.98, 19.94.

^{15}N NMR (41 MHz, -60 °C, CD_2Cl_2): δ 821.50 (s, *anti*, $MesCH_2S^{15}NO$), δ 756.10 (s, *syn*, $MesCH_2S^{15}NO$). ^{15}N NMR (41 MHz, 10 °C, CD_2Cl_2): δ 764.823 (s, *syn*, $MesCH_2S^{15}NO$) (Figure S7).

UV-Vis (CH_2Cl_2, 25 °C): λ_{max}/nm (ε/$M^{-1}cm^{-1}$) = 549 (52), 517 (21) (Figure S8).

FT-IR (cm^{-1}): 1484 ν(^{14}NO); 630 ν(S-^{14}N); 1461 ν(^{15}NO); 614 ν(S-^{15}N); Hooke's law predicts $^{15N/14N}\Delta\nu$ = 27 cm^{-1} and $^{15N/14N}\Delta\nu$ = 16, respectively (Figure S9). The IR spectra were taken by putting $MesCH_2SNO$ as a dense oil directly on the ATR instrument.

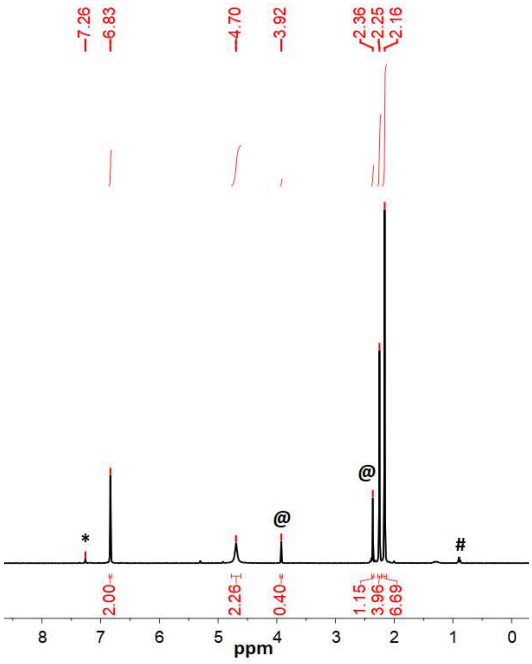

Figure S6. ^{1}H NMR spectrum (400 MHz, 25 °C, $CDCl_3$) of $MesCH_2SNO$ (**2**). The resonances marked with (*) and (#) are from the solvent residual peak for chloroform-d_1 and pentane, respectively. The resonances marked with (@) is from $MesCH_2SSCH_2Mes$ formed due to the decomposition of $MesCH_2SNO$.

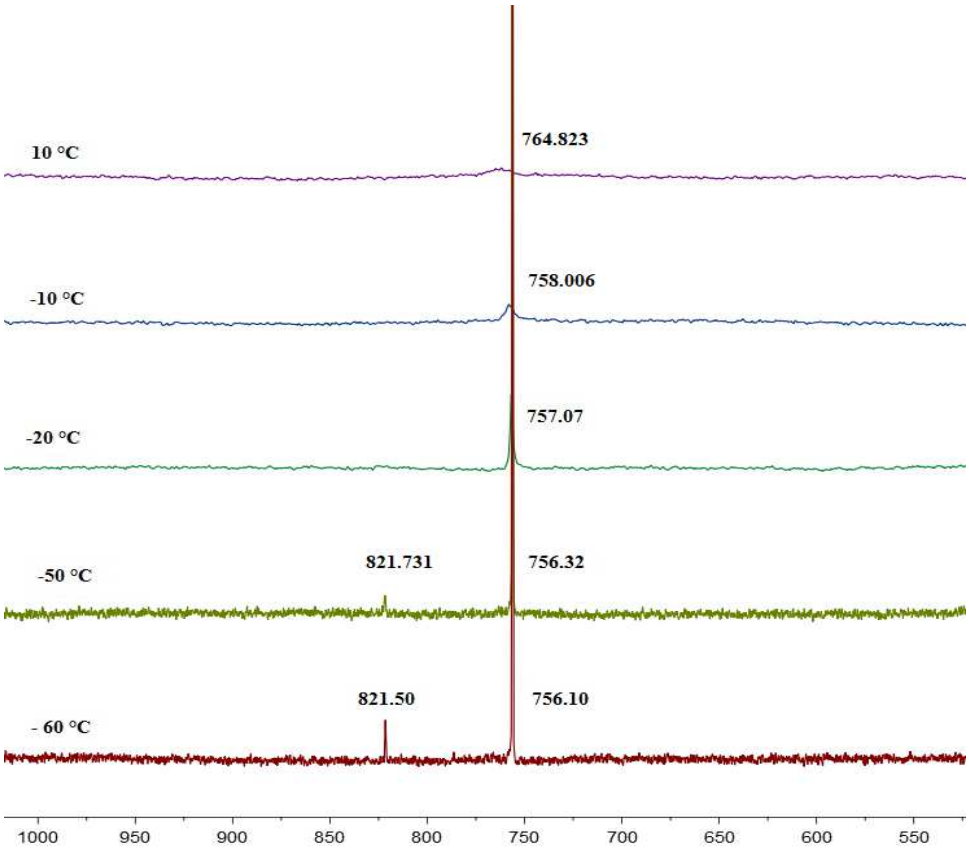

Figure S7. Variable temperature ^{15}N NMR spectra (41 MHz, CD_2Cl_2) of $MesCH_2S^{15}NO$ (**2-^{15}N**).

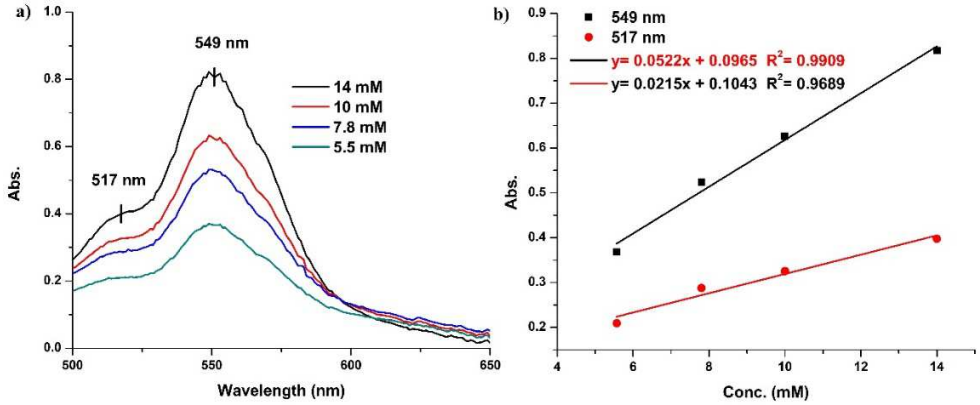

Figure S8. a) UV-Vis spectra of $MesCH_2SNO$ (**2**) in dichloromethane at 25 °C at different concentrations. b) Beer's law plot for (**2**) depicts λ_{max} = 517 nm (ε =21 $M^{-1}cm^{-1}$) and λ_{max} = 549 nm (ε = 52 $M^{-1}cm^{-1}$).

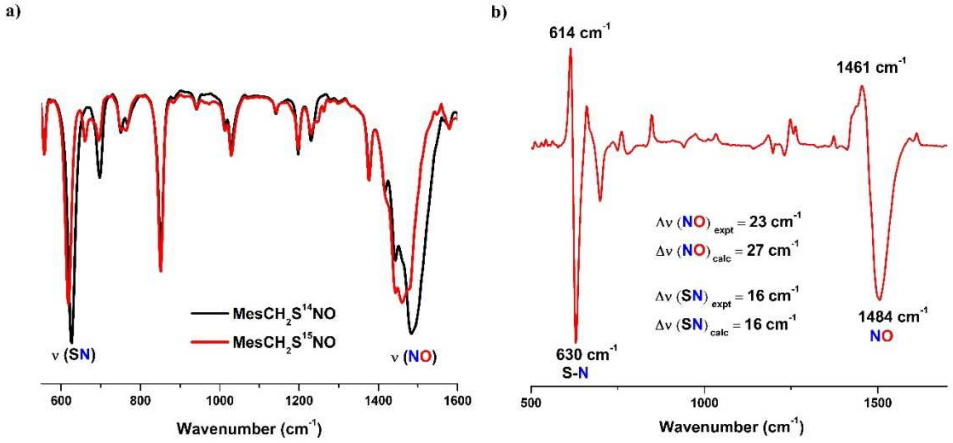

Figure S9. a) FT-IR spectra of $MesCH_2S^{14}NO$ (**2**) (black trace) and $MesCH_2S^{15}NO$ (**2**-^{15}**N**) (red trace). b) The difference spectrum between (**2**) (down) and (**2**-^{15}**N**) (up).

5. Synthesis and Characterization of AdSNO-B(C_6F_5)$_3$ (3)

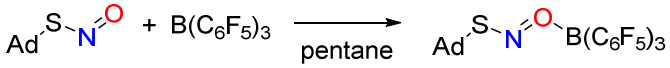

Scheme S3. Synthesis of AdSNO-B(C_6F_5)$_3$ (**3**).

A solution of B(C_6F_5)$_3$ (0.259 g, 0.506 mmol) in pentane (5 mL) was added to a solution of AdSNO (0.1 g, 0.506 mmol) in pentane (2 mL). The color of the solution immediately changed from dark green to yellow. The solution was concentrated to ca. 3 mL and kept at -40 °C to give the product (0.29 g, 80% yield) as yellow color crystals.

^{1}H NMR (400 MHz, 298 K, $CDCl_3$): δ 2.35 (d, 6H, CH_2), 2.29 (m, 3H, C*H*), 1.87 (d, 6H, CH_2) (Figure S10).

^{19}F NMR (376 MHz, 298 K, $CDCl_3$): δ -131.36 (m, 6F), -151.38 (m, 3F), -162.45 (m, 6F) (Figure S11).

^{13}C{^{1}H} NMR (100 MHz, 233.15 K, $CDCl_3$): *δ* 147.72 (m), 140.64 (m), 137.68 (m), 114.93 (m), 65.53, 42.76(minor), 42.08(major), 37.04(minor), 35.89(minor), 35.30(minor), 35.05(major), 29.76(minor), 29.52(major), 29.03(minor) (Figure S12).

^{15}N NMR (41 MHz, -60 °C, CD_2Cl_2): δ 740.59 (s, *O-anti*-AdS^{15}NO-B(C_6F_5)$_3$), 681.25 (s, *O-syn*-AdS^{15}NO-B(C_6F_5)$_3$), 553.49 (s, *N-syn*-AdS^{15}NO-B(C_6F_5)$_3$) (Figure S13).

UV-Vis (CH_2Cl_2, 25 °C): λ_{max}/nm (ε/M^{-1}cm^{-1}) = 510 (9) (Figure S15).

FT-IR (X, cm^{-1}): 1257 ν(^{14}NO); 853 ν(S-^{14}N); 1237 ν(^{15}NO); 835 ν(S-^{15}N); Hooke's law predicts $^{15N/14N}\Delta\nu$ = 24 cm^{-1} and $^{15N/14N}\Delta\nu$ = 20, respectively (Figure S16). The IR spectra were taken by putting AdSNO-B(C_6F_5)$_3$ as a fine powder directly on the ATR instrument. Anal. Calcd for $C_{28}H_{15}BF_{15}NOS$ (**3**): C, 47.42; H, 2.13; N, 1.97. Found: C, 47.55; H, 2.48; N, 1.34. The lower experimental value for N arises from loss of NO from AdSNO-BCF due to its thermal instability.

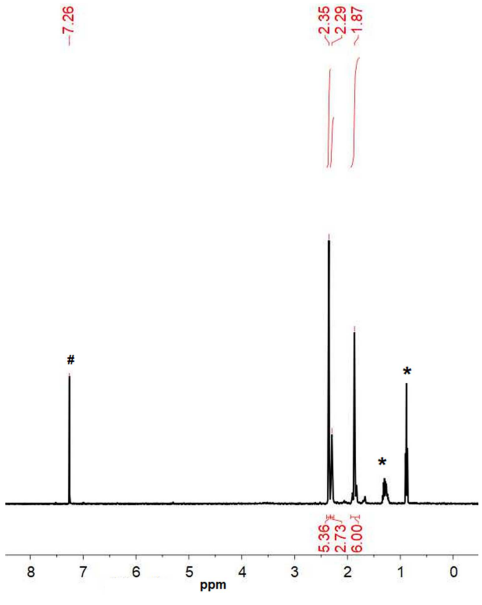

Figure S10. ^{1}H NMR spectrum (400 MHz, 25 °C, $CDCl_3$) of AdSNO-BCF (**3**). The resonances marked with (*) and (#) are from the solvent residual peak pentane and chloroform-d_1, respectively.

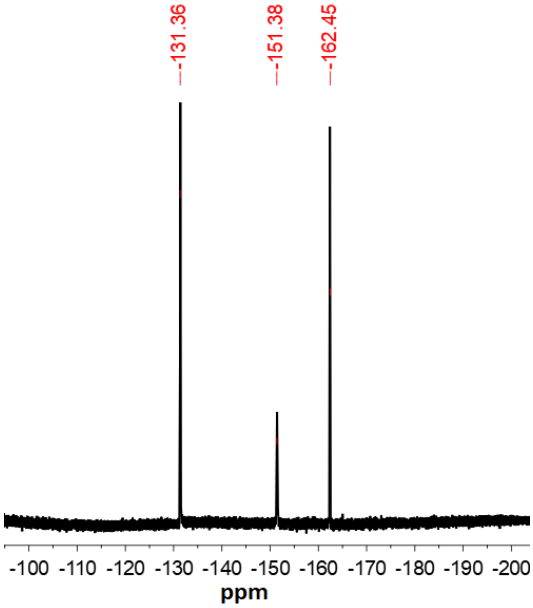

Figure S11. ^{19}F NMR spectrum (376 MHz, 25 °C, $CDCl_3$) of AdSNO-BCF (**3**).

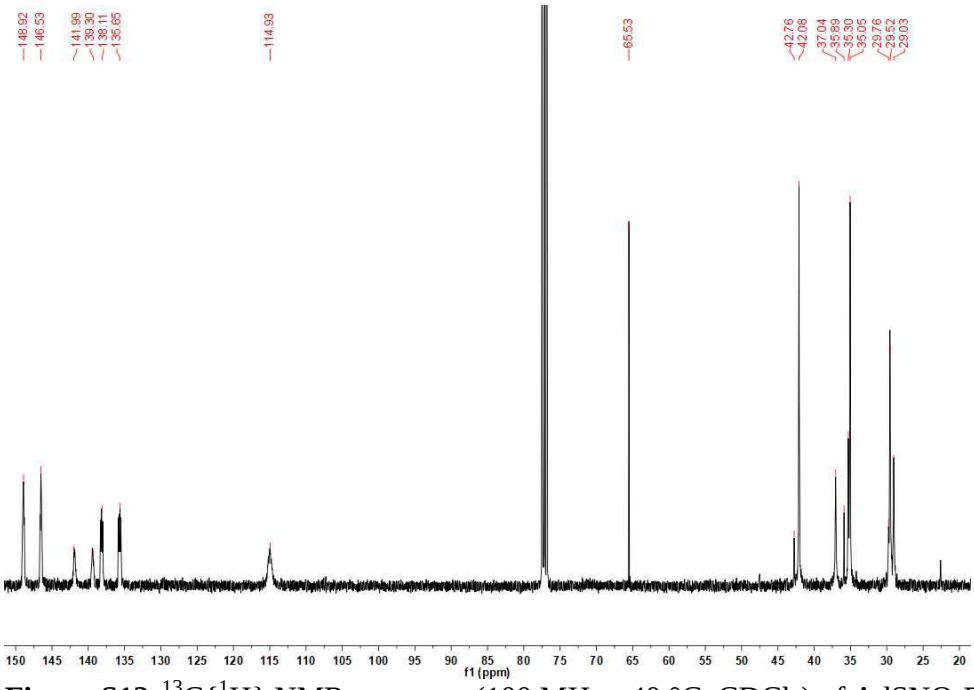

Figure S12. ^{13}C{^{1}H} NMR spectrum (100 MHz, -40 °C, $CDCl_3$) of AdSNO-BCF (**3**).

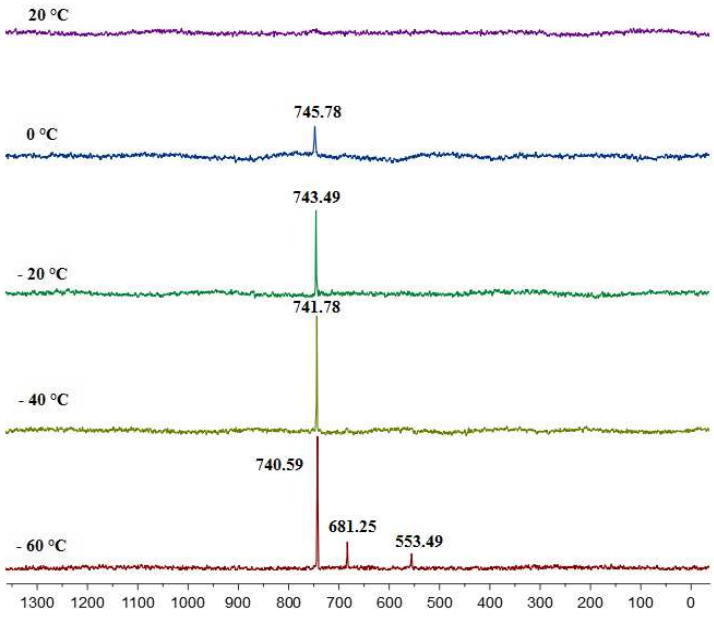

Figure S13. Variable temperature ^{15}N NMR spectra (41 MHz, CD_2Cl_2) of Ad$S^{15}NO$-$B(C_6F_5)_3$ (**3-^{15}N**).

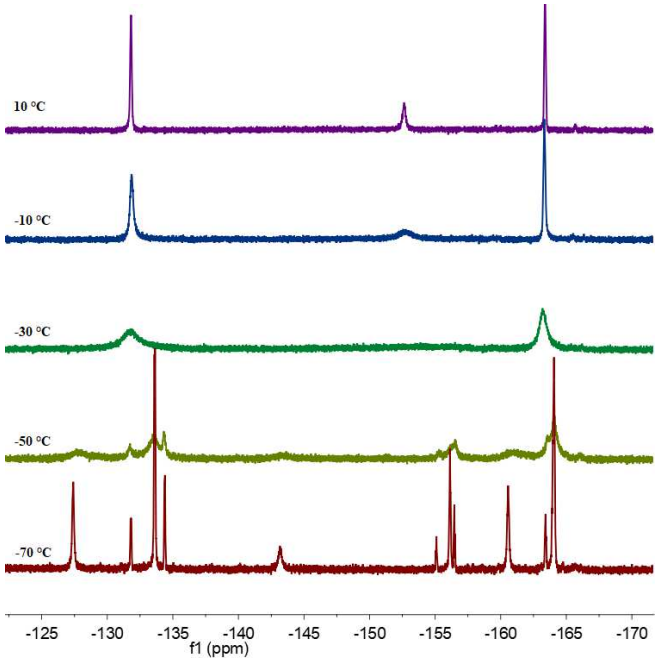

Figure S14. Variable temperature ^{19}F NMR spectra (376 MHz, CD_2Cl_2) of Ad$S^{15}NO$-$B(C_6F_5)_3$ (**3-^{15}N**).

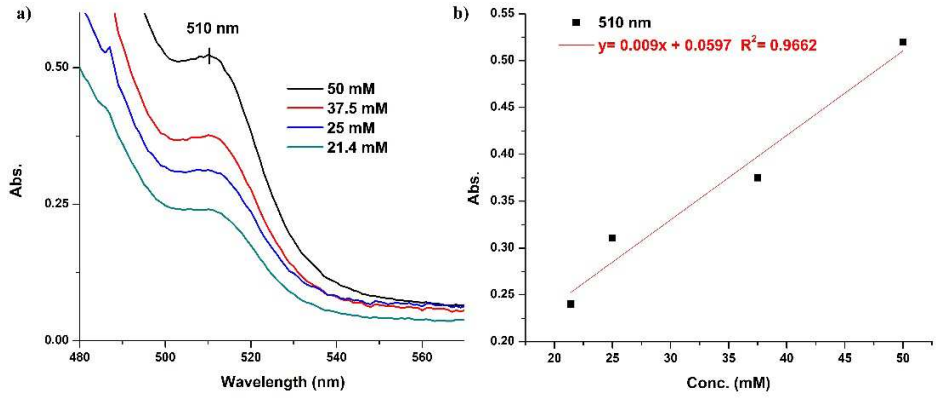

Figure S15. a) UV-Vis spectra of AdSNO-B(C_6F_5)$_3$ (**3**) in dichloromethane at 25 °C at different concentrations. b) Beer's law plot for (**3**) depicts λ_{max} = 510 nm (ε = 9 $M^{-1}cm^{-1}$).

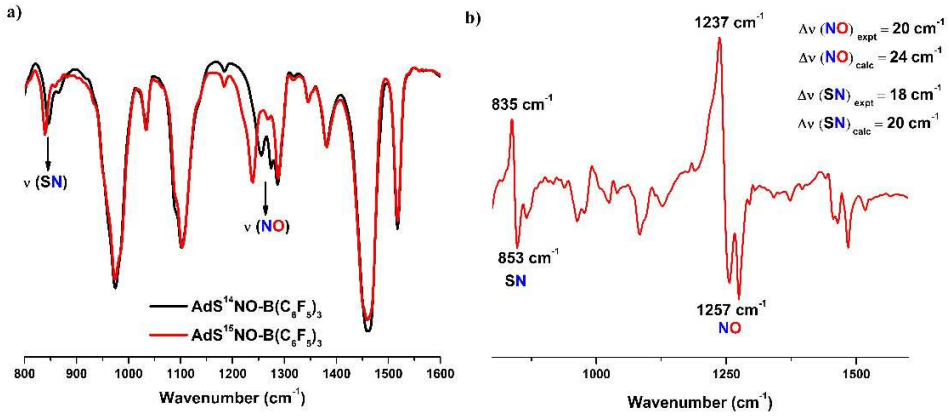

Figure S16. a) FT-IR spectra of Ads^{14}NO-B(C_6F_5)$_3$ (**3**) (black trace) and Ads^{15}NO-B(C_6F_5)$_3$ (**3**-^{15}**N**) (red trace). b) The difference spectrum between (**3**) (down) and (**3**-^{15}**N**) (up).

6. Synthesis and Characterization of $MesCH_2SNO$-$B(C_6F_5)_3$ (4)

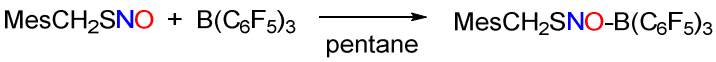

Scheme S4. Synthesis of $MesCH_2SNO$-$B(C_6F_5)_3$ (**4**).

A solution of $B(C_6F_5)_3$ (0.262 g, 0.512 mmol) in pentane (5 mL) was added to a solution of $MesCH_2SNO$ (0.1 g, 0.512 mmol) in pentane (2 mL). The color of the solution immediately changed from pink to orange. The solution was concentrated to ca. 3 mL and kept at -40 °C to yield to give the product (0.26 g, 71% yield) as orange crystals.

^{1}H NMR (400 MHz, 298 K, $CDCl_3$): δ 6.87 (s, 2H, Aryl-CH), 4.79 (s, 2H, CH_2), 2.26 (s, 3H, CH_3), 2.18 (s, 6H, CH_3) (Figure S17).

^{19}F NMR (376 MHz, 298 K, $CDCl_3$): δ -129.93 (m, 6F), -148.16 (m, 3F), -161.36 (m, 6F) (Figure S18).

^{13}C{^{1}H} NMR (100 MHz, 233.15 K, $CDCl_3$): δ 147.81 (m), 140.44(s), 140.81 (m), 138.45(s), 137.01(m), 130.08(s), 118.19(s), 114.69(m), 41.48(s), 21.21(s, minor), 21.21(s, major), 20.16(s, minor), 20.09(s, major) (Figure S19).

^{15}N NMR (41 MHz, -70 °C, CD_2Cl_2): δ 678.24 (s), 553.97 (s), 231.756 (s) (Figure S20).

UV-Vis (CH_2Cl_2, 25 °C): λ_{max}/nm (ε/$M^{-1}cm^{-1}$) = 481 (40) (Figure S22).

FT-IR (X, cm^{-1}): 1282 ν(^{14}NO); 863 ν(S-^{14}N); 1261 ν(^{15}NO); 845 ν(S-^{15}N); Hooke's law predicts $^{15N/14N}\Delta\nu$ = 25 cm^{-1} and $^{15N/14N}\Delta\nu$ = 20, respectively (Figure S23). The IR spectra were taken by putting $MesCH_2SNO$-$B(C_6F_5)_3$ as a fine powder directly on the ATR instrument.

Anal. Calcd for $C_{28}H_{13}BF_{15}NOS$ (**4**): C, 47.55; H, 1.85; N, 1.98. Found: C, 47.58; H, 2.08; N, 1.05. The lower experimental value for N arises from loss of NO from $MesCH_2SNO$-BCF due to its thermal instability.

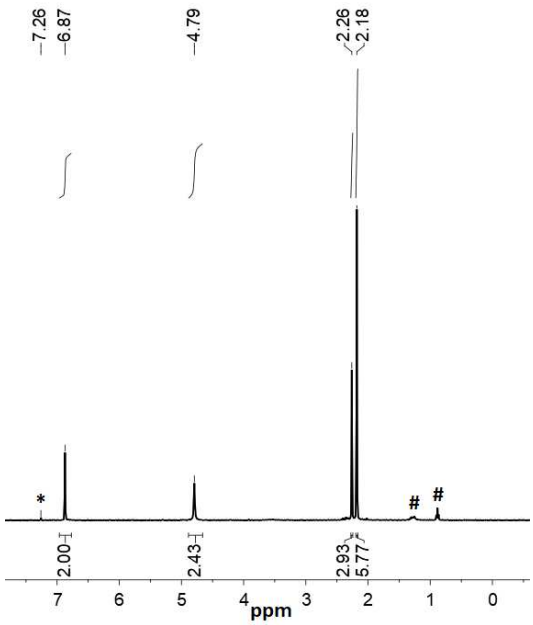

Figure S17. ^{1}H NMR spectrum (400 MHz, 25 °C, $CDCl_3$) of $MesCH_2SNO$-BCF (**4**). The resonances marked with (*) and (#) are from the solvent residual peak for chloroform-d_1 and pentane, respectively.

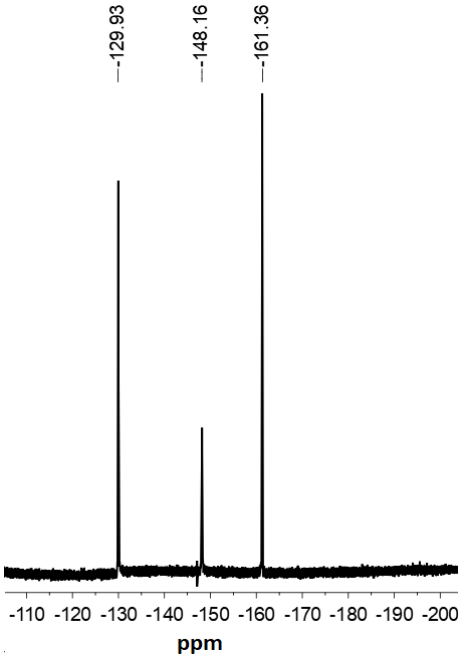

Figure S18. ^{19}F NMR spectrum (376 MHz, 25 °C, $CDCl_3$) of $MesCH_2SNO$-BCF (**4**).

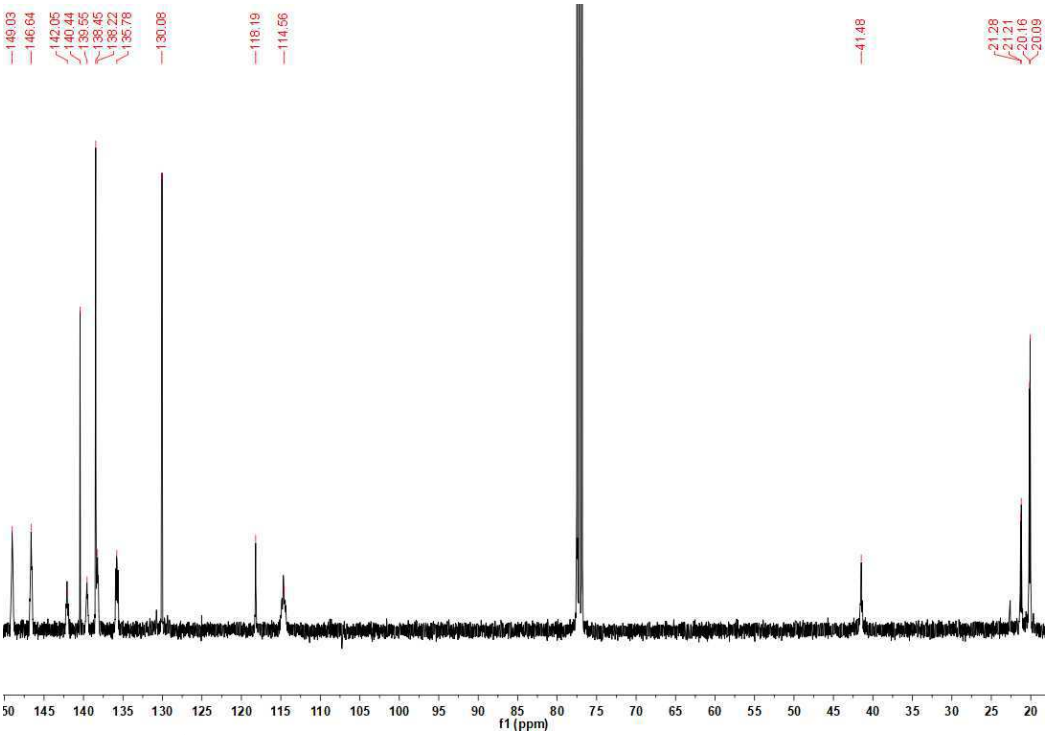

Figure S19. $^{13}C\{^{1}H\}$ NMR spectrum (100 MHz, -40 °C, $CDCl_3$) of $MesCH_2SNO$-BCF (**4**).

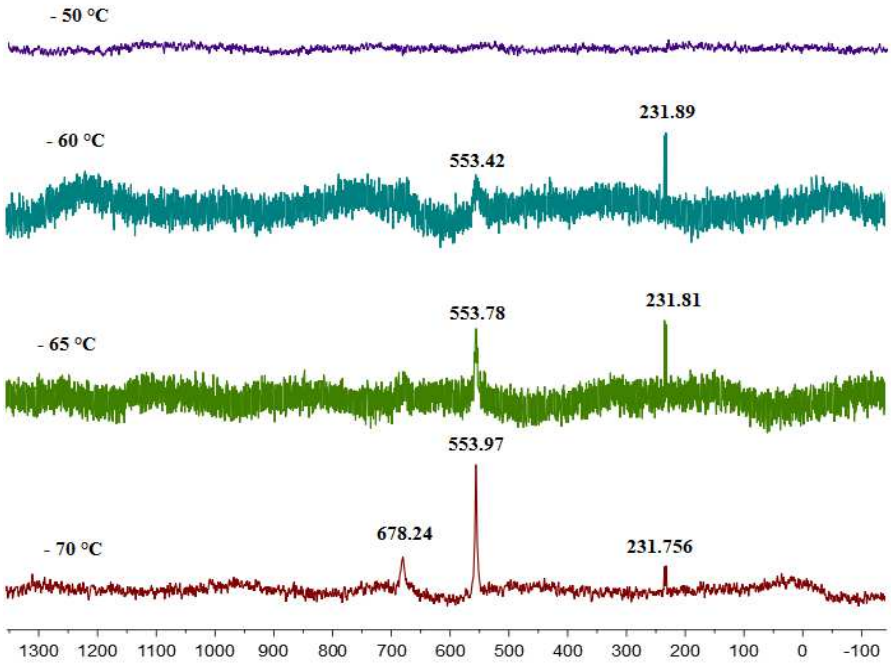

Figure S20. Variable temperature ^{15}N NMR spectra (41 MHz, CD_2Cl_2) of $MesCH_2S^{15}NO\text{-}B(C_6F_5)_3$ (**4**-^{15}**N**).

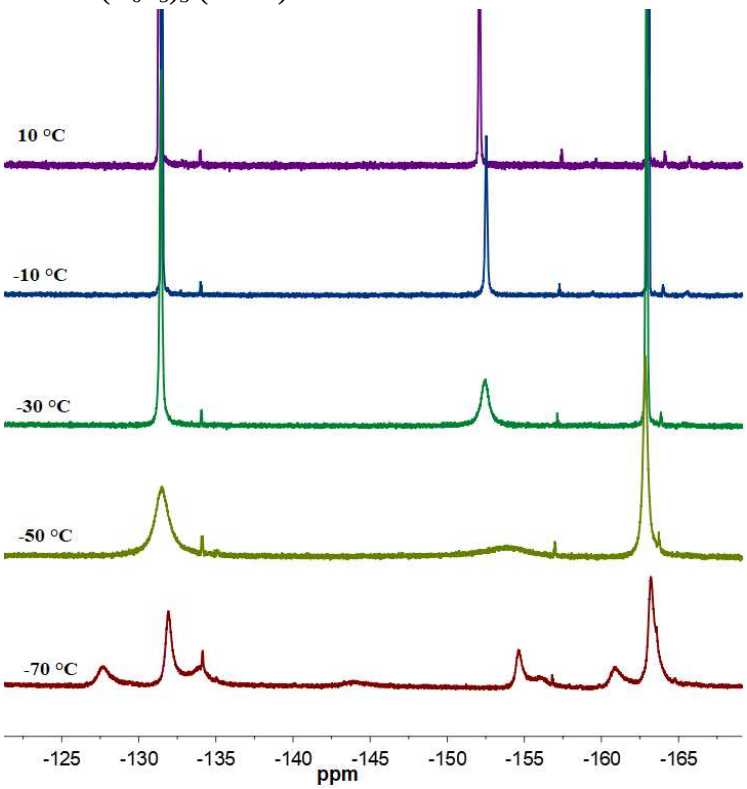

Figure S21. Variable temperature ^{19}F NMR spectra (376 MHz, CD_2Cl_2) of $MesCH_2SNO\text{-}BCF$ (**4**).

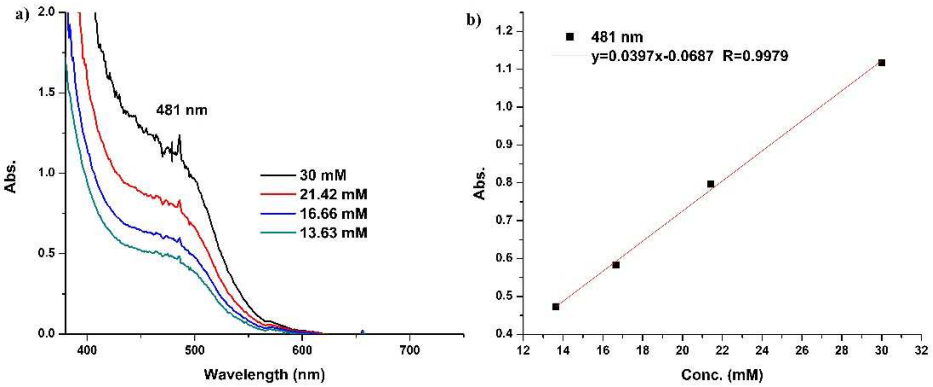

Figure S22. a) UV-Vis spectra of $MesCH_2SNO\text{-}B(C_6F_5)_3$ (**4**) in dichloromethane at 25 °C at different concentrations. b) Beer's law plot for (**4**) depicts λ_{max}/nm (ε/$M^{-1}cm^{-1}$) = 481 (40).

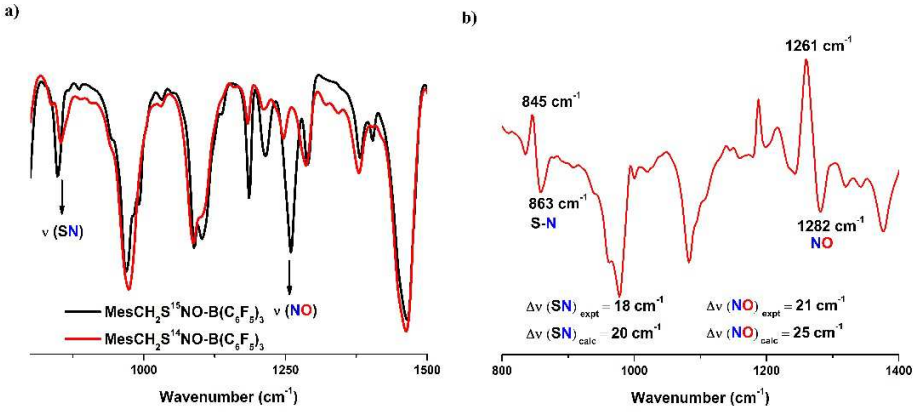

Figure S23. a) FT-IR spectra of $MesCH_2S^{14}NO$ (**4**) (red trace) and $MesCH_2S^{15}NO$ **(4-^{15}N)** (black trace). b) The subtracted spectrum of (**4**) (down) and (**4-^{15}N**) (up).

7. Cyclic Voltammetry Measurements

General Considerations. Cyclic voltammetry measurements were done at room temperature under dry nitrogen atmosphere of a glove-box using a BASi Epsilon Electrochemistry setup with three electrodes (Working electrode: glassy carbon, Auxiliary electrode: platinum wire, Pseudo-reference electrode: silver/silver nitrate). As a non-coordinating electrolyte tetrabutylammonium teraphenylborate was used for all cyclic voltammetry measurements.

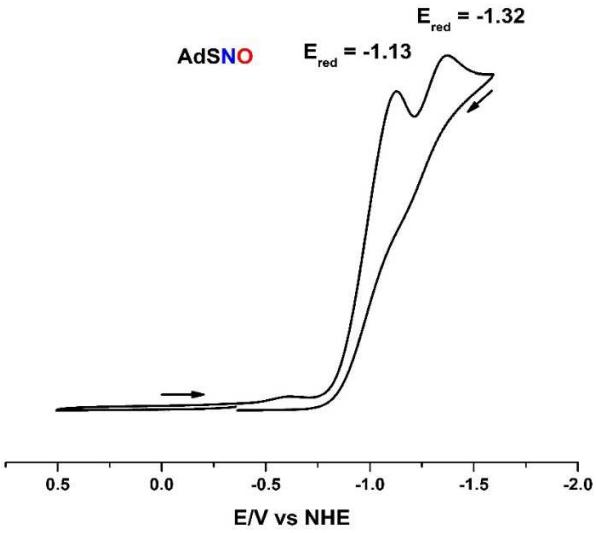

Figure S24. Cyclic voltammetry of Ad-SNO (**1**) (7 mM) in dichloromethane at 25 °C in presence of $[Bu_4N][BPh_4]$ (0.1 M) with the scan rate of 50 mV/s.

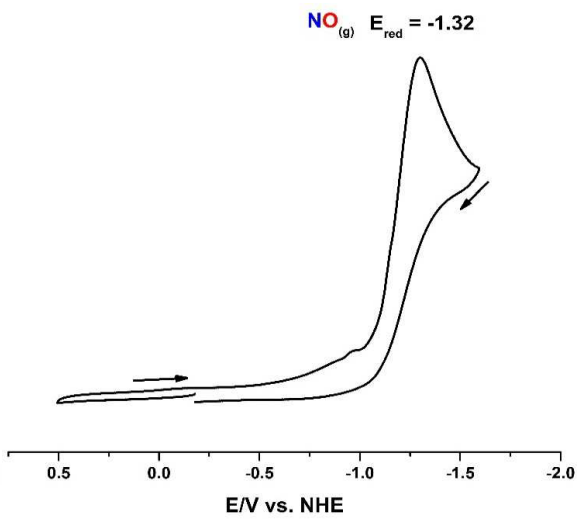

Figure S25. Cyclic voltammetry of NO gas (saturated solution) in dichloromethane at 25 °C in presence of $[Bu_4N][BPh_4]$ (0.1 M).

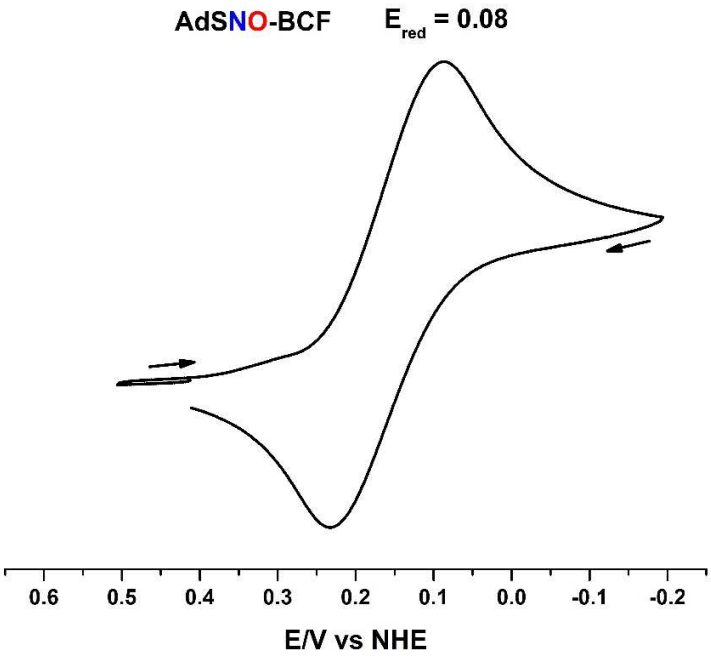

Figure S26. Cyclic voltammetry of AdSNO-B(C_6F_5)$_3$ (**3**) (7 mM) in dichloromethane at 25 °C in presence of [Bu_4N][BPh_4] (0.1 M) with the scan rate of 50 mV/s.

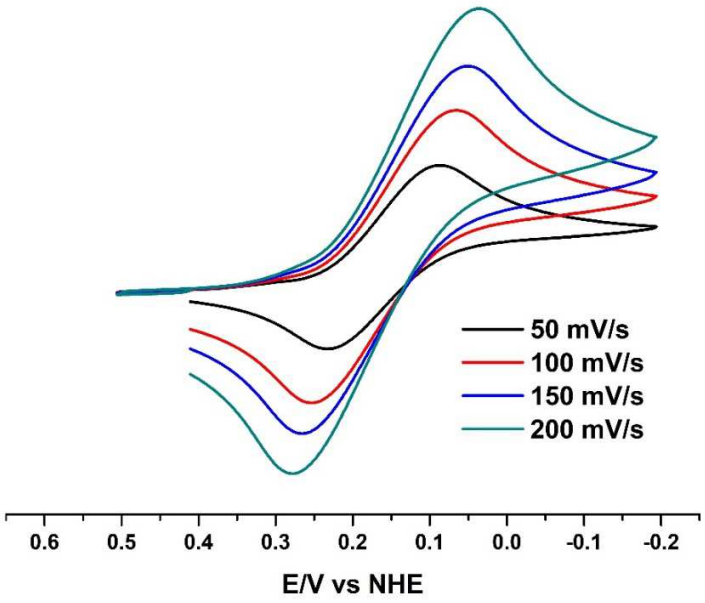

Figure S27. Cyclic voltammetry of AdSNO-B(C_6F_5)$_3$ (**3**) (7 mM) in dichloromethane at 25 °C in presence of [Bu_4N][BPh_4] (0.1 M) at different scan rates.

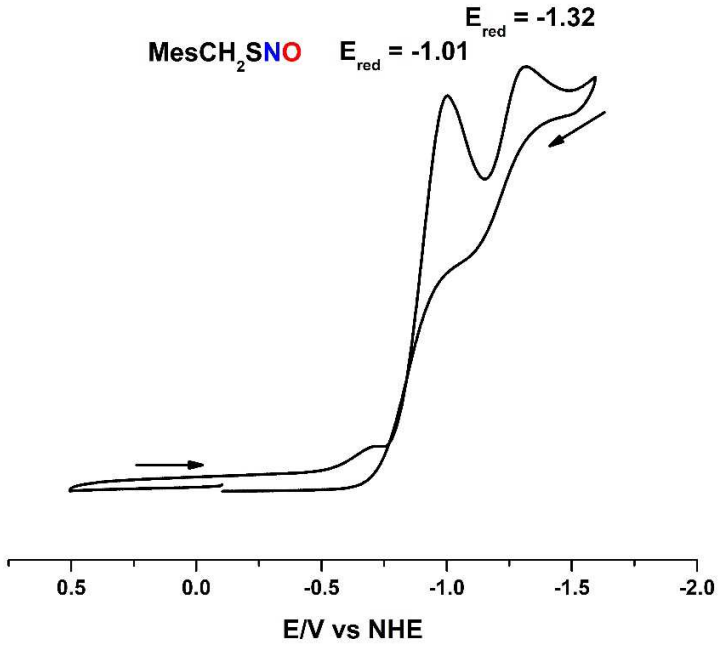

Figure S28. Cyclic voltammetry of $MesCH_2SNO$ (**2**) (7 mM) in dichloromethane at 25 °C in presence of $[Bu_4N][BPh_4]$ (0.1 M) with the scan rate of 50 mV/s.

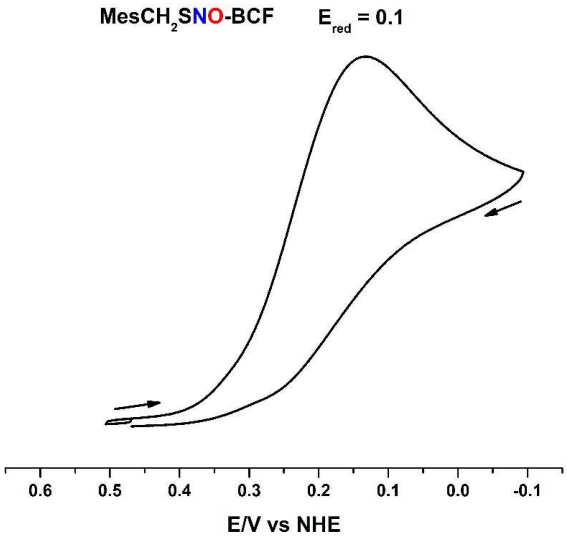

Figure S29. Cyclic voltammetry of $MesCH_2SNO\text{-}B(C_6F_5)_3$ (**4**) (7 mM) in dichloromethane at 25 °C in presence of $[Bu_4N][BPh_4]$ (0.1 M) with the scan rate of 50 mV/s.

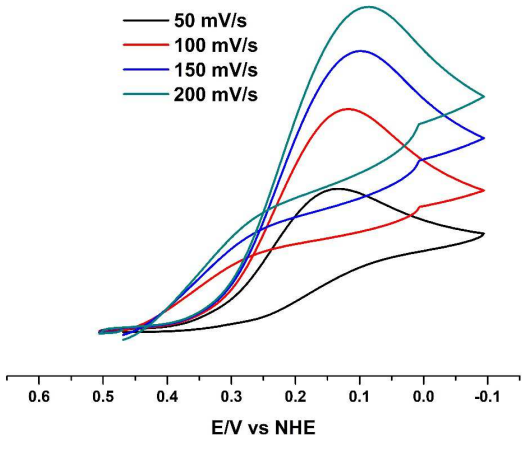

Figure S30. Cyclic voltammetry of $MesCH_2SNO\text{-}B(C_6F_5)_3$ (**4**) (7 mM) in dichloromethane at 25 °C in presence of $[Bu_4N][BPh_4]$ (0.1 M) at different scan

8. Reduction of AdSNO (1) with Cp^*_2Co

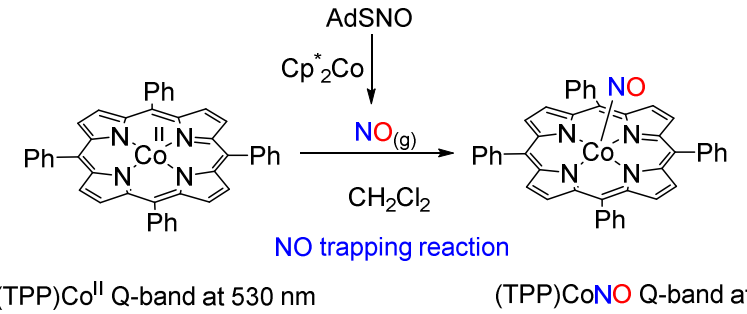

Scheme 5. Trapping NO released from reaction of AdSNO (**1**) with Cp^*_2Co by $(TPP)Co^{II}$.

Quantitative trapping of nitric oxide was done using Cobalt(II)-meso-tetraphenylporphine [$(TPP)Co^{II}$] which was purchased from Strem Chemical and used for a similar experimental set up as previously described.[3] AdSNO (**1**) (1.0 mL, 10.0 mM) was weighed in a small vial and placed in a larger vial. The lager vial was sealed with a septum. A solution of $(TPP)Co^{II}$ complex (10.0 mL, 1.0 mM) in dichloromethane was injected to the big vial. Then a solution of decamethylcobaltocene (1.0 mL, 10.0 mM) in fluorobenzene was injected to the inner vial and the solutions in both vials stirred for 1 hr. Then an aliquot (100 μL) of the resultant (TPP)Co solution from outer vial was diluted to 2.0 mL using CH_2Cl_2 and analyzed by UV-Vis spectroscopy. The Q-band absorption features in the UV-Vis spectra of authentic $(TPP)Co^{II}$ (530 nm) and (TPP)Co(NO) (540 nm) samples were used to compare and quantify the yield of cobalt-nitrosyl species.

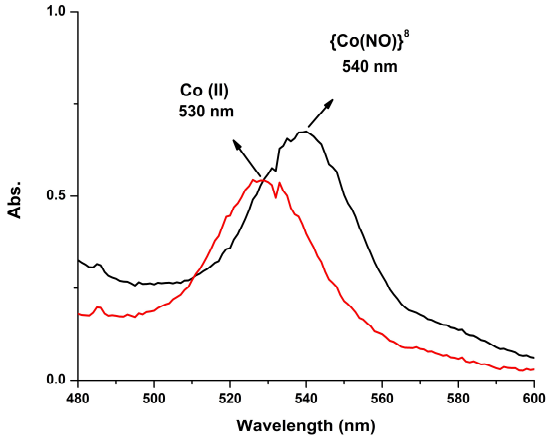

Figure S31. UV-Vis spectra (in CH_2Cl_2 at 25 °C) of (TPP)Co (red trace) and (TPP)Co(NO) (black trace) species generated from the reaction of $(TPP)Co^{II}$ with NO released from the reaction of AdSNO (**1**) with Cp^*_2Co. The yield of NO formation is 82%.

9. Reduction of $MesCH_2SNO$ (2) with Cp^*_2Co

Decamethylcobaltocene (1.0 mL 10.0 mM) in fluorobenzene was added to $MesCH_2SNO$ (**2**) (1 mL, 10 mM) in fluorobenzene and the solution stirred for 5 h. Formation of NO from the reaction of $MesCH_2SNO$ (**2**) and decamethylcobaltocene was quantitatively measured by employing $(TPP)Co^{II}$ complex as a NO trap in 71% yield.

10. Reduction of AdSNO-$B(C_6F_5)_3$ (3) with Cp^*_2Co

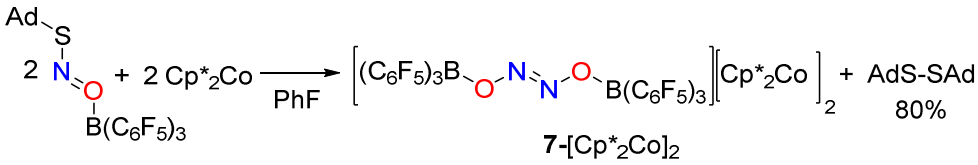

Scheme S6. Reduction of AdSNO-BCF (**3**) with Cp^*_2Co.

A solution of decamethylcobaltocene (0.046 g, 0.141 mmol) in fluorobenzene (3 mL) was added to a solution of AdSNO-BCF (**3**) (0.1 g, 0.141 mmol) in fluorobenzene (2 mL). The color of the solution immediately changed from yellow to dark yellow. The solution was evaporated, and the resulting dark yellow solid was washed with pentane. The solid was then dissolved in 3 mL dichloromethane and was layered with cold pentane and kept at -40 °C to give the product $[(C_6F_5)_3B\text{-}ON{=}NO\text{-}B(C_6F_5)_3][Cp^*_2Co]_2$ (**7**-$[Cp^*_2Co]_2$) (0.180 g, 73% yield) as yellow crystals. ^1H NMR analysis on the yellow solution indicates the formation of free disulfide in 80% yield via its ^1H NMR spectrum (400 MHz, 298 K, $CDCl_3$): δ 2.06 (br, 6H, CH_2-Ad), 1.82 (br, 12H, CH_2-Ad), 1.67 (br, 12H, CH_2-Ad).

Characterization data for **7**-$[Cp^*_2Co]_2$

^1H NMR (400 MHz, 298 K, $CDCl_3$): δ 1.60 (s, 30H) (Figure S32).

$^{13}C\{^1H\}$ NMR (100 MHz, 233.15 K, CD_2Cl_2): δ 147.69 (m), 138.42 (m), 136.11 (m), 123.28(m), 93.84, 7.87.

^{19}F NMR (376 MHz, 298 K, $CDCl_3$): δ -132.29 (m, 6F), -163.57 (m, 3F), -167.17 (m, 6F) (Figure S33).

^{15}N NMR (41 MHz, -40 °C, CD_2Cl_2): δ 429.91, δ 384.93 (Figure S34).

UV-Vis (CH_2Cl_2, 25 °C): λ_{max}/nm (ε/$M^{-1}cm^{-1}$) = 340 (1575), 405 (344) (Figure S35).

FT-IR (X, cm^{-1}): 1010 $\nu(^{14}NO)$; 987 $\nu(^{15}NO)$; Hooke's law predicts $^{15N/14N}\Delta\nu$ = 19 cm^{-1} (Figure S36). The IR spectra were taken as a thin film by evaporating a dichloromethane solution of **7**-$[Cp^*_2Co]_2$ on a KBr window.

Anal. Calcd for $C_{76}H_{60}B_2Co_2F_{30}N_2O_2$ (**7**-$[Cp^*_2Co]_2$): C, 52.38; H, 3.47; N, 1.61. Found: C, 52.22; H, 3.49; N, 1.55.

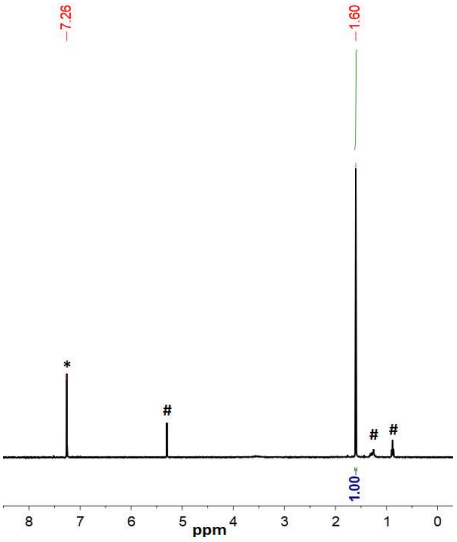

Figure S32. ^1H NMR spectrum (400 MHz, 25 °C, $CDCl_3$) of $[(C_6F_5)_3B\text{-}ON{=}NO\text{-}B(C_6F_5)_3][Cp^*_2Co]_2$ (**7**-$[Cp^*_2Co]_2$). The resonances marked with (*) and (#) are from the solvent residual peak for chloroform-d_1 and pentane, respectively.

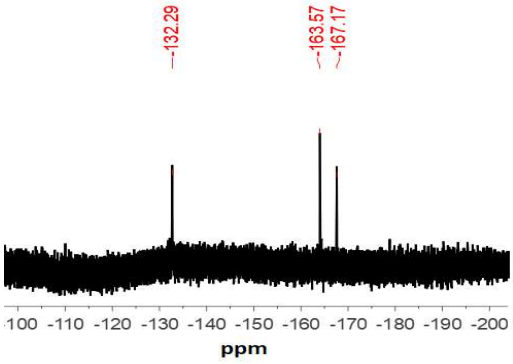

Figure S33. ^{19}F NMR spectrum (376 MHz, 25 °C, $CDCl_3$) of $[(C_6F_5)_3B\text{-}ON{=}NO\text{-}B(C_6F_5)_3][Cp^*_2Co]_2$ (**7**-$[Cp^*_2Co]_2$).

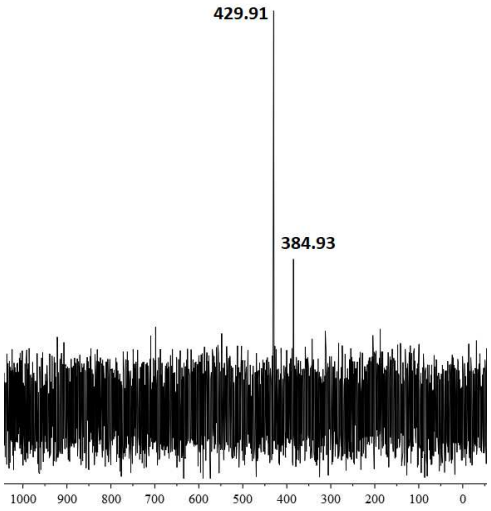

Figure S34. ^{15}N NMR spectrum (41 MHz, CD_2Cl_2) of $[(C_6F_5)_3B\text{-}ON{=}NO\text{-}B(C_6F_5)_3][Cp^*_2Co]_2$ (**7**-$[Cp^*_2Co]_2$) at -

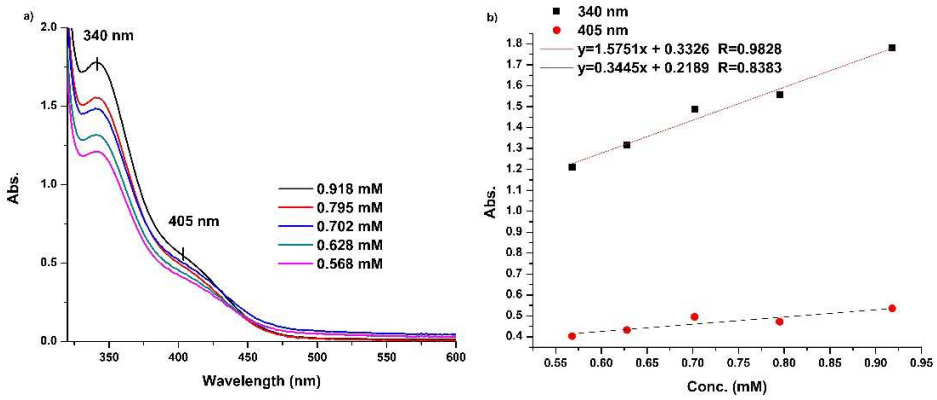

Figure S35. a) UV-Vis spectra of $[(C_6F_5)_3B\text{-}ON{=}NO\text{-}B(C_6F_5)_3][Cp^*_2Co]_2$ at 25 °C (**7**-$[Cp^*_2Co]_2$) in dichloromethane at 25 °C at different concentrations. b) Beer's law plot for (**7**-$[Cp^*_2Co]_2$) depicts λ_{max}/nm (ε/$M^{-1}cm^{-1}$) = 340 (1575).

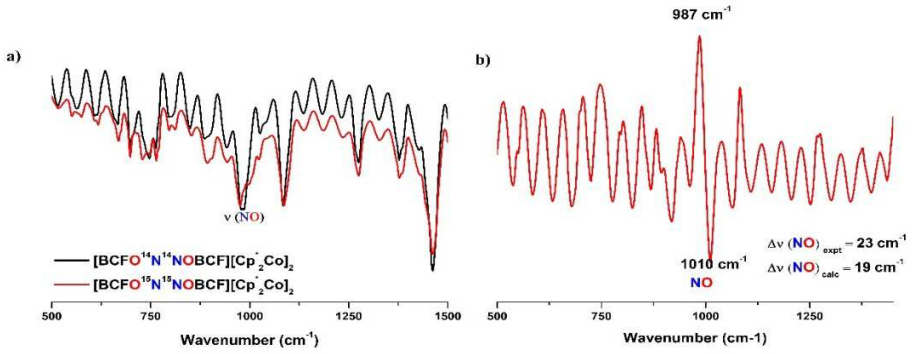

Figure S36. a) FT-IR spectra of $[(C_6F_5)_3B\text{-}O^{14}N{=}^{14}NO\text{-}B(C_6F_5)_3][Cp_2{}^*Co]_2$ (**7**-$[Cp^*_2Co]_2$) (black trace) and $[(C_6F_5)_3B\text{-}O^{15}N{=}^{15}NO\text{-}B(C_6F_5)_3][Cp^*_2Co]_2$ (**7**-$[Cp^*_2Co]_2$-**^{15}N**) (red trace). b) The subtracted spectrum of (**7**-$[Cp^*_2Co]_2$) (down) and (**7**-$[Cp^*_2Co]_2$-**^{15}N**) (up).

11. Reduction of $MesCH_2SNO$-BCF (4) with Cp^*_2Co

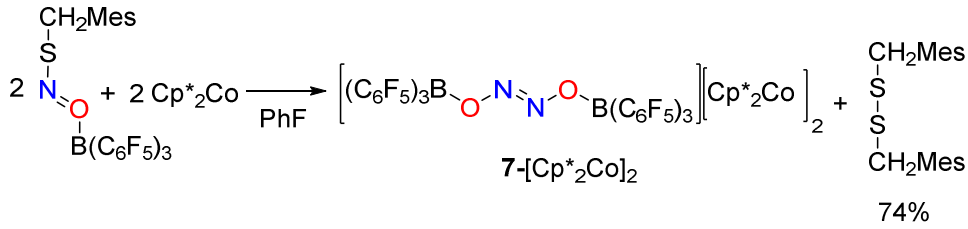

Scheme S7. Reduction of $MesCH_2SNO$-BCF (**4**) with Cp^*_2Co.

A solution of decamethylcobaltocene (0.046 g, 0.141 mmol) in fluorobenzene (3 mL) was added to a solution of $MesCH_2SNO$-BCF (**4**) (0.1 g, 0.141 mmol) in fluorobenzene (2 mL). The color of the solution immediately changed from orange to dark yellow. The solution was evaporated, and the resulting dark yellow solid was washed with pentane. The solid was then dissolved in 3 mL dichloromethane and filtered through celite to give a clear solution which was layered with cold pentane and kept at -40 °C to give the product $[(C_6F_5)_3B\text{-}O^{15}N=^{15}NO\text{-}B(C_6F_5)_3][Cp^*_2Co]_2$ (**7**-$[Cp^*_2Co]_2$) (0.160 g, 65% yield) as yellow crystals. ^{1}H NMR analysis on the yellow solution indicates the formation of free disulfide in 74% yield via its ^{1}H NMR spectrum (400 MHz, 298 K, $CDCl_3$): δ 6.83 (s, 2H, Aryl-CH), 3.92 (s, 2H, CH_2), 2.36 (s, 3H, CH_3), 2.24 (s, 6H, CH_3).

Reduction of AdSNO-$B(C_6F_5)_3$ (3) with Cp_2Fe

A solution of ferrocene (0.026 g, 0.141 mmol) in dichloromethane (3 mL) was added to a solution of AdSNO-BCF (**3**) (0.1 g, 0.141 mmol) in dichloromethane (2 mL). The color of the solution immediately changed from yellow to purple. The solution was evaporated, and the resulting purple solid was washed with pentane. The solid was then dissolved in 3 mL fluorobenzene and was layered with cold pentane and kept at -40 °C to give the product $[(C_6F_5)_3B\text{-}ON=NO\text{-}B(C_6F_5)_3][Cp_2Fe]_2$ (**7**-$[Cp_2Fe]_2$) (0.145 g, 70% yield) as purple crystal.

Scheme S8. Reduction of AdSNO-BCF (**3**) with Cp_2Fe.

13. Reduction of $MesCH_2SNO\text{-}B(C_6F_5)_3$ (4) with Cp_2Fe

A solution of ferrocene (0.026 g, 0.141 mmol) in dichloromethane (3 mL) was added to a solution of $MesCH_2SNO$-BCF (**4**) (0.1 g, 0.141 mmol) in dichloromethane (2 mL). The color of the solution immediately changed from orange to purple. The solution was evaporated, and the resulting purple solid was washed with pentane. The solid was then dissolved in 3 mL fluorobenzene and was layered with cold pentane and kept at -40 °C to give the product $[(C_6F_5)_3B\text{-}ON{=}NO\text{-}B(C_6F_5)_3][Cp_2Fe]_2$ (**7**-$[Cp_2Fe]_2$) (0.130 g, 63% yield) as purple crystals.

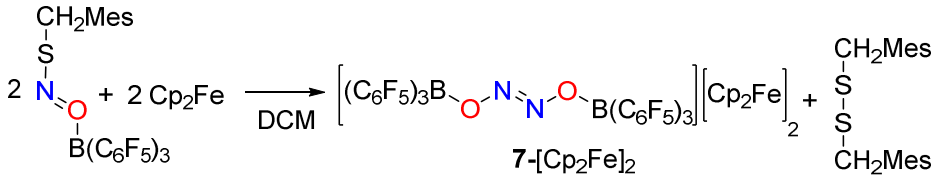

Scheme S9. Reduction of $MesCH_2SNO$-BCF (**4**) with Cp_2Fe.

14. EPR Analysis for the Reduction of ASNO-B(C_6F_5)$_3$ (3) with Cp^*_2Co

A fluorobenzene solution of decamethylcobaltocene (10 mM, 0.5 ml) in an EPR tube was slowly layered with a pentane solution of AdSNO-BCF (**3**) (23 mM, 0.217 ml) at RT. The EPR tube was capped and transferred outside the glovebox without shaking. The tube was then shaken couple of times and quickly placed in the EPR instrument.

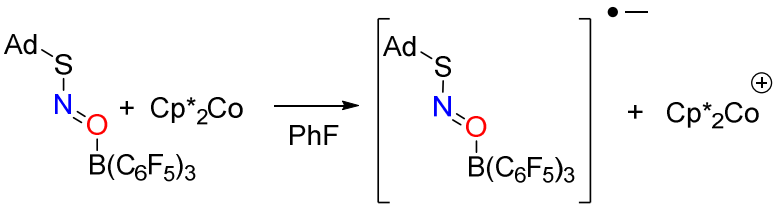

5

Scheme 10. Reduction of AdSNO-BCF (**3**) with Cp^*_2Co to generate [AdSNO-BCF]$^{\bullet/-}$ (**5**).

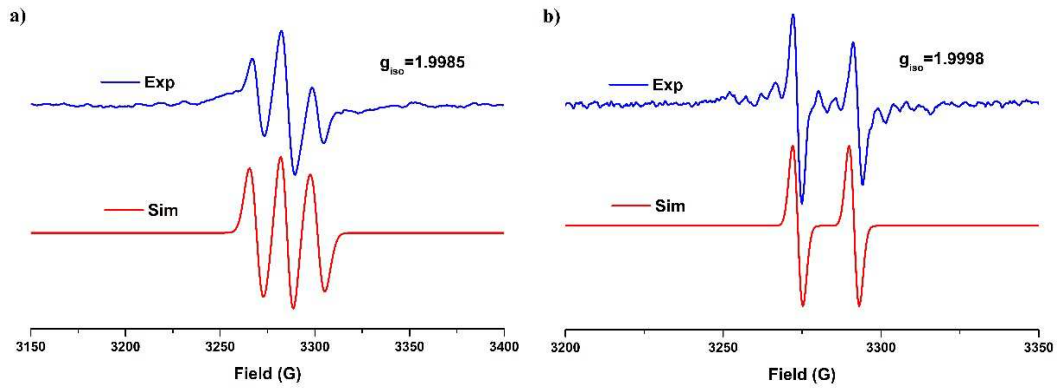

Figure S37. Isotropic X-band EPR spectra (blue trace) and simulation (red trace) of the reaction between (a) AdSNO-BCF (**3**) or (b) AdS^{15}NO-BCF (**3-^{15}N**) and Cp^*_2Co to generate radical anions **5-^{14}N** and **5-^{15}N**, respectively, in a mixture of fluorobenzene/pentane at 25 °C. Frequency =9.194384 GHz, power = 0.99 mW, ModWidth = 15 mT, time-constant = 0.03 s. Simulation provides g_{iso} = 1.9985, A_{iso}(^{14}N) = 45.0 MHz and W_{iso} = 2.7 mT (for **3**), and g_{iso} = 1.9998, A_{iso}(^{15}N) = 62.5 MHz, W_{iso} = 2.1 mT (for **3-^{15}N**). As expected, the ratio of isotropic ^{15}N and ^{14}N hyperfine coupling constants A(^{15}N)/A(^{14}N) = 1.38 is very close to the ratio of their gyromagnetic ratios γ(^{15}N)/γ(^{14}N) =1.40.

15. Crystallographic Details and Additional Structures

Single crystals of each compound AdSNO-B(C_6F_5)$_3$ (**3**) (CCDC 1945525), MesCH_2SNO-B(C_6F_5)$_3$ (**4**) (CCDC 1945527), [(C_6F_5)$_3$B-ON=NO-B(C_6F_5)$_3$][Cp^*_2Co]$_2$ (**7**-[Cp^*_2Co]$_2$) (CCDC 1945528), [(C_6F_5)$_3$B-ON=NO-B(C_6F_5)$_3$][Cp_2Fe]$_2$ (**7**-[Cp_2Fe]$_2$) (CCDC 1945529) were mounted under mineral oil on a Mitegen micromount and immediately placed in a cold nitrogen stream at 100(2) K prior to data collection. Data for compounds **3**, **7**-[Cp^*_2Co]$_2$, and **7**-[Cp_2Fe]$_2$ were collected on a Bruker D8 Quest equipped with a Photon100 CMOS detector and a Mo ImS source. Data for **4** were collected on a Bruker DUO equipped with an APEXII CCD detector and Mo fine-focus sealed source. A series of 0.5^o φ- and ω-scans were collected with monochromatic Mo Kα radiation, λ = 0.7107 Å and integrated with the Bruker SAINT program. Structure solution and refinement was performed using the SHELXTL/PC suite and ShelXle. Intensities were corrected for Lorentz and polarization effects and an empirical absorption correction was applied using Blessing's method as incorporated into the program SADABS. Non-hydrogen atoms were refined with anisotropic thermal parameters and hydrogen atoms were included in idealized positions unless otherwise noted. Further comments on structural models:

[AdSNO-BCF] (C_5H_{12})$_{0.5}$ (3). One half occupied lattice pentane solvent molecule is present in the lattice. This molecule is disordered across a symmetry site. The like C-C distances were restrained to be similar.

[(C_6F_5)$_3$B-ON=NO-B(C_6F_5)$_3$][Cp_2^*Co]$_2$ (7-[Cp^*_2Co]$_2$**).** A total of eight highly disordered fluoro-benzene solvent molecules per unit cell were removed from the model using the SQUEEZE routine in PLATON. Attempts to model the disordered solvent molecules resulted in non-convergence, thus they were removed.

[(C_6F_5)$_3$B-ON=NO-B(C_6F_5)$_3$][Cp_2Fe]$_2$ (7-[Cp_2Fe]$_2$**).** The data was refined as a two component twin. The ratio of the twin domains refined to ~69:31, and the twin law by rows was (-1 0 0), (0 -1 0), (.113 0 1). Two C6F5 groups are disordered over two orientations. The like C-F and C-C distances were restrained to be similar. The C1/C1B and C31/C31B atom pairs were constrained to have equal x,y,z positions and equal anisotropic displacement parameters.

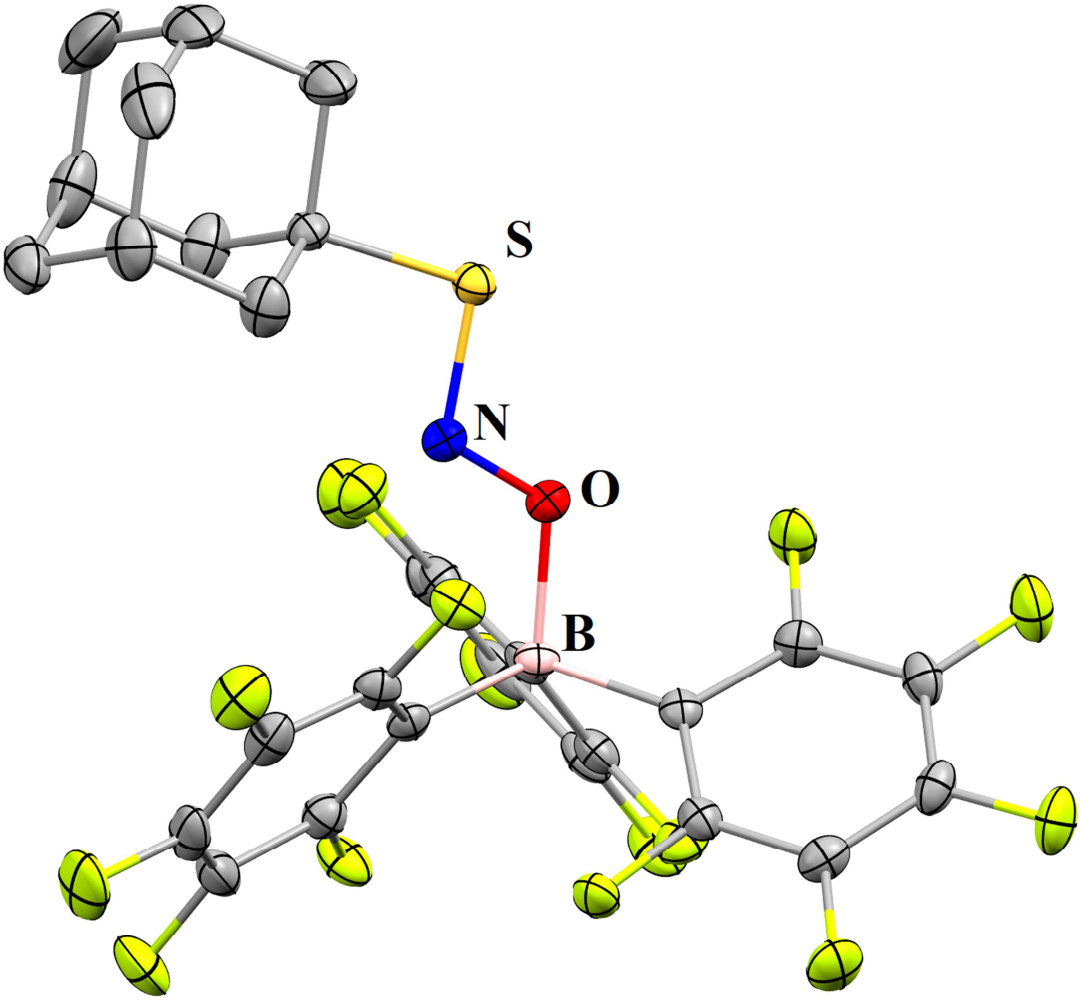

Figure S38. Molecular structure of AdSNO-BCF (**3**) (CCDC 1945525). The thermal ellipsoid plots are drawn at 50% probability level. Hydrogen atoms are omitted for clarity. Selected bond distances (Å) and angles (°): S-N 1.6252(17), N-O 1.278(2), O-B 1.612(3), S-N-O 112.37(13), N-O-B 118.74(14).

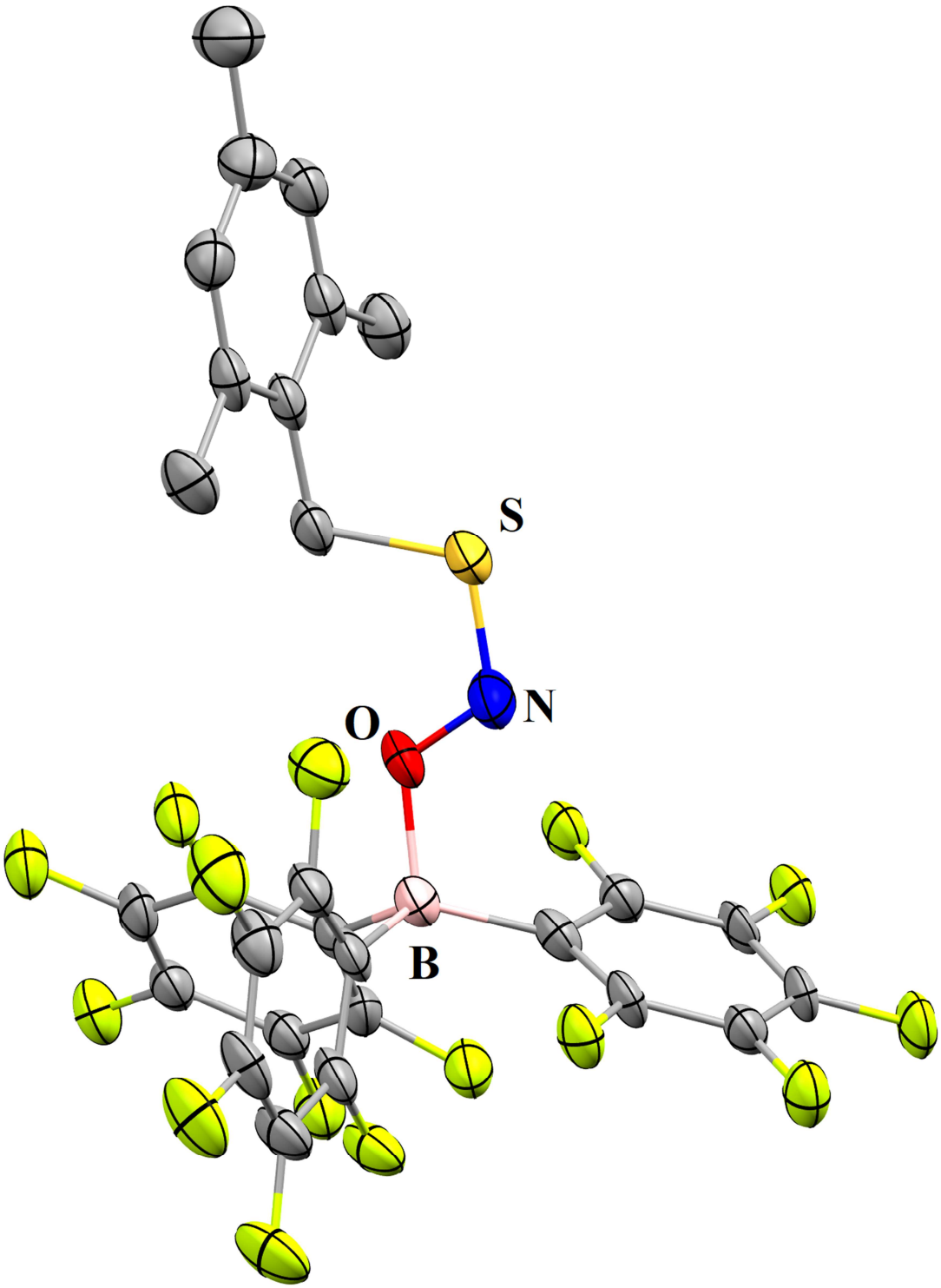

Figure S39. Molecular structure of $MesCH_2SNO$-BCF (**4**) (CCDC 1945527). The thermal ellipsoid plots are drawn at 50% probability level. Hydrogen atoms are omitted for clarity. Selected bond distances (Å) and angles (°): S-N 1.608(5), N-O 1.274(5), O-B 1.586(7), S-N-O 116.0(4), N-O-B 116.9(4).

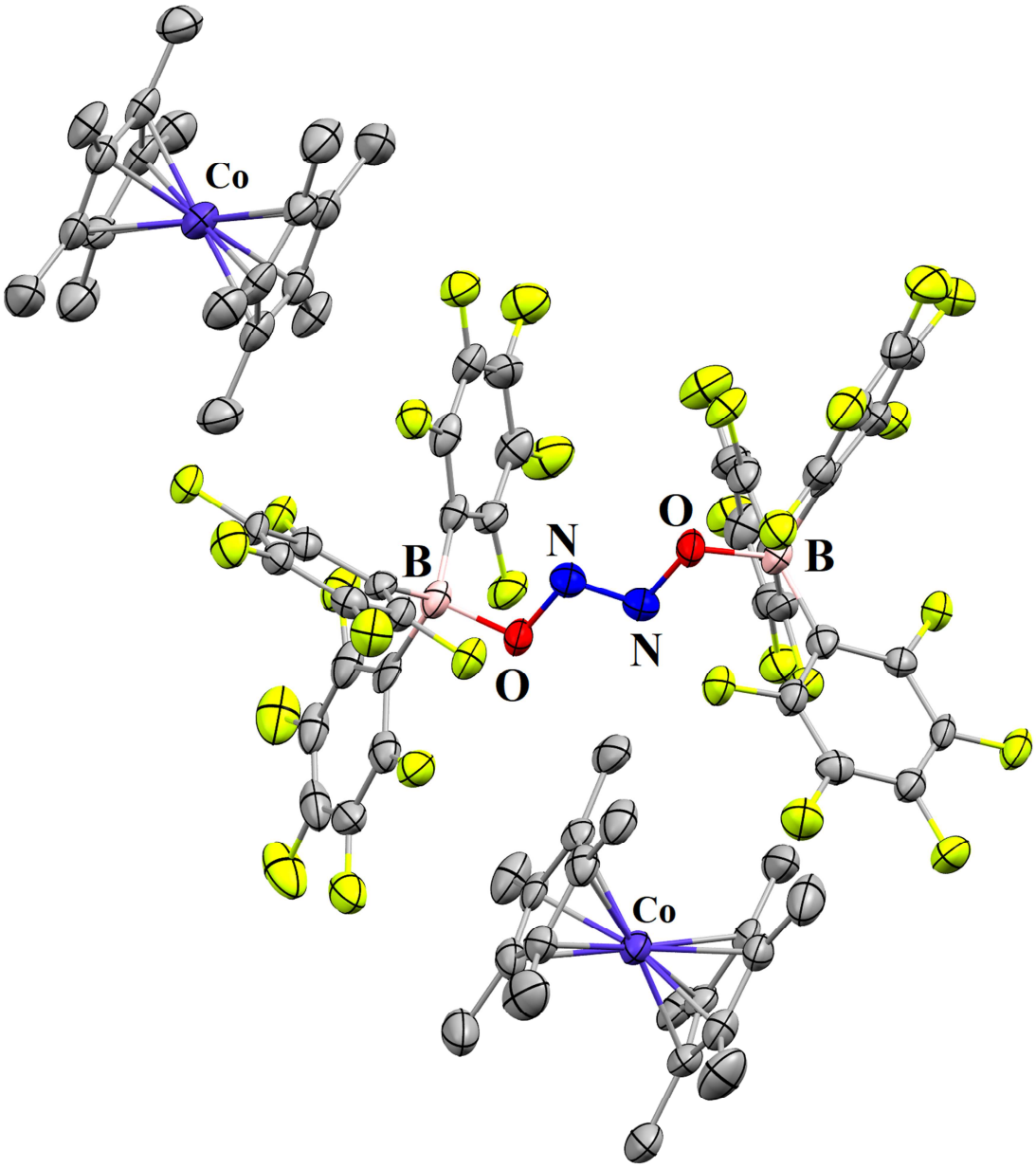

Figure S40. Molecular structure of $[(C_6F_5)_3B\text{-}ON{=}NO\text{-}B(C_6F_5)_3][Cp^*_2Co]_2$ (**7**-$[Cp^*_2Co]_2$) (CCDC 1945528). The thermal ellipsoid plots are drawn at 50% probability level. Hydrogen atoms are omitted for clarity. Selected bond distances (Å) and angles (°): N-O 1.381(6), N-N 1.257(9), O-B 1.489(7), O-N-N 106.5(5), N-O-B 109.0(4).

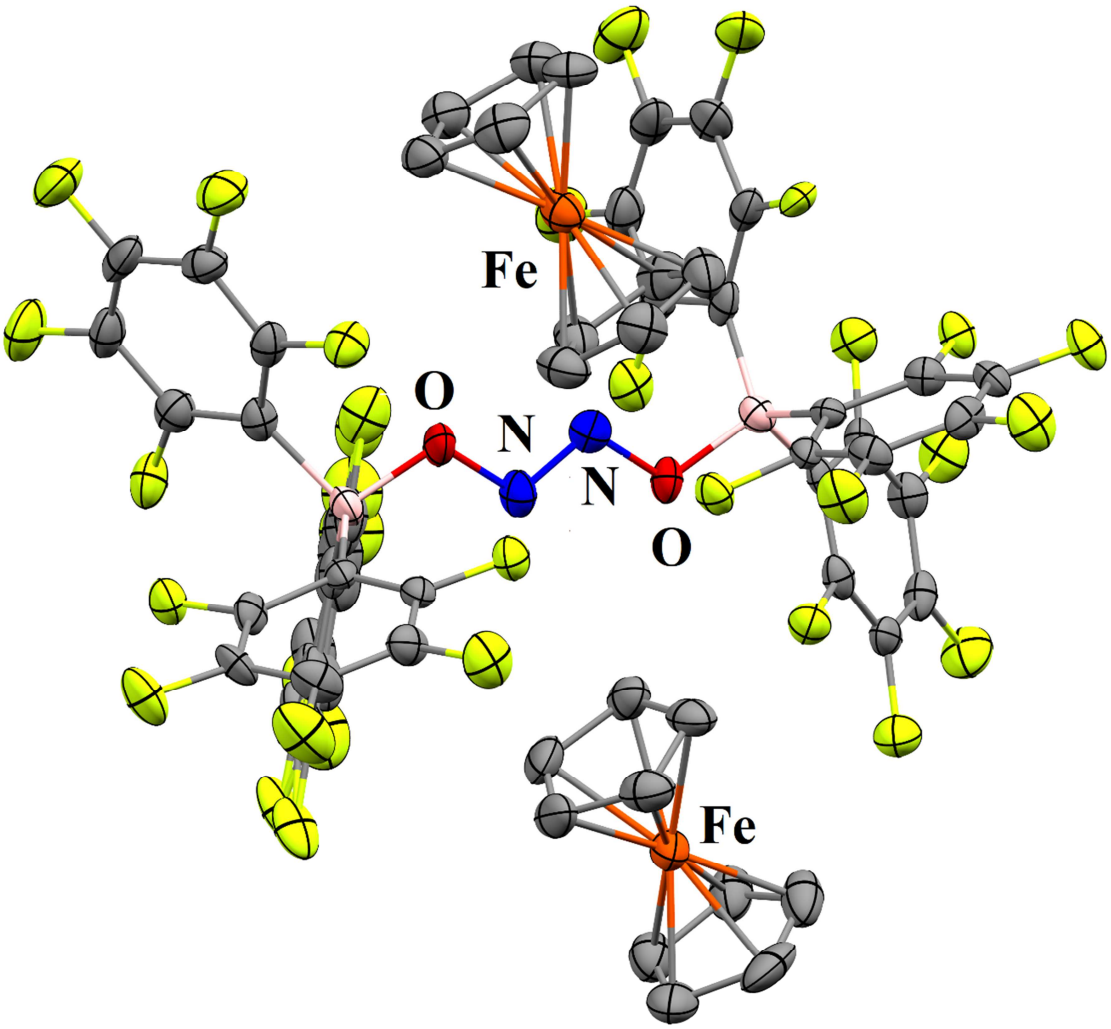

Figure S41. Molecular structure of $[(C_6F_5)_3B\text{-}ON{=}NO\text{-}B(C_6F_5)_3][CpFe]_2$ (**7**-$[Cp_2Fe]_2$) (CCDC 1945529). The thermal ellipsoid plots are drawn at 50% probability level. Hydrogen atoms are omitted for clarity. Selected bond distances (Å) and angles (°): N1-O1 1.380 (4), N2-O2 1.364 (4), N1-N2 1.274 (4), O1-B1 1.492(6), O2-B2 1.505(6), N1-O1-B1 113.8 (4), N2-O2-B2 111.9 (3), N2-N1-O1 107.0 (4), N1-N2-O2 106.3 (4).

16. Computational Details and Results

Electronic structure calculations were performed using density functional theory (DFT) with ωB97XD range-separated density functional with empirical dispersion correction;[4] previous benchmarking of the performance of the DFT methods for the RSNO compounds against high-level ab inito results[5] demonstrated a good performance of the ωB97XD functional for description of the –SNO group properties. A triple-zeta quality basis set augmented with diffuse functions, ma-def2-TZVPP, has been used throughout; preliminary calculations also employed smaller ma-def2-SV(P) basis set.[6-7] Due to the system size, calculations of structures including more than one $B(C_6F_5)_3$ moieties (Figures S46-S48) used a reduced ma-def2-SV(P) basis set, red-ma-def2-SV(P), with removed diffuse and polarization basis functions on F atoms and removed diffuse functions on C atoms.

Solvent (dichloromethane) effects have been treated using the integral equation formalism polarizable continuum model (IEFPCM) as implemented in Gaussian 16.[8]

Harmonic frequency calculations have been performed for all optimized structures to ascertain the nature of the stationary point found; thermodynamic parameters have been calculated within harmonic approximation for the T=298 K, 1 M standard state.

NMR chemical shifts were calculated with the standard Gauge-Independent Atomic Orbital (GIAO) method.[9] Atomic spin populations were evaluated with Natural Population Analysis (NPA).[10]

The relative contributions of the resonance structures ***S***, ***D***, and ***I*** (Figure 1A in the main text) have been estimated using Natural Resonance Theory (NRT) approach as implemented in the NBO 7.0 code.[11-15] The NRT calculations used a local NRT variant, where only the resonance structures arising from the –SNO group have been considered. To ensure consistency of the NRT results across the different molecules/complexes, the three resonance structures ***S***, ***D***, and ***I*** have been used as the reference structures for the NRT calculation and the NRTPAR parameter has been set to 99%.

Cartesian coordinates for calculated structures may be found in an accompanying supporting information file.

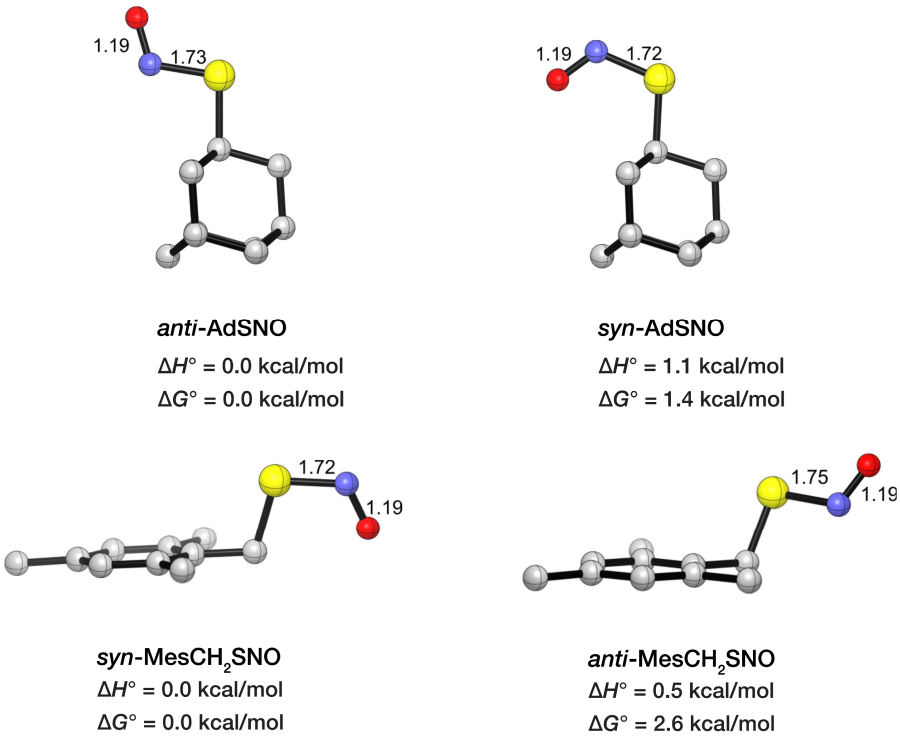

Figure S42. Structures and relative free energies of AdSNO and $MesCH_2SNO$ conformers calculated at the ωB97XD-PCM(CH_2Cl_2)/ma-def2-TZVPP level. Bond lengths in Å; hydrogen atoms not shown for clarity.

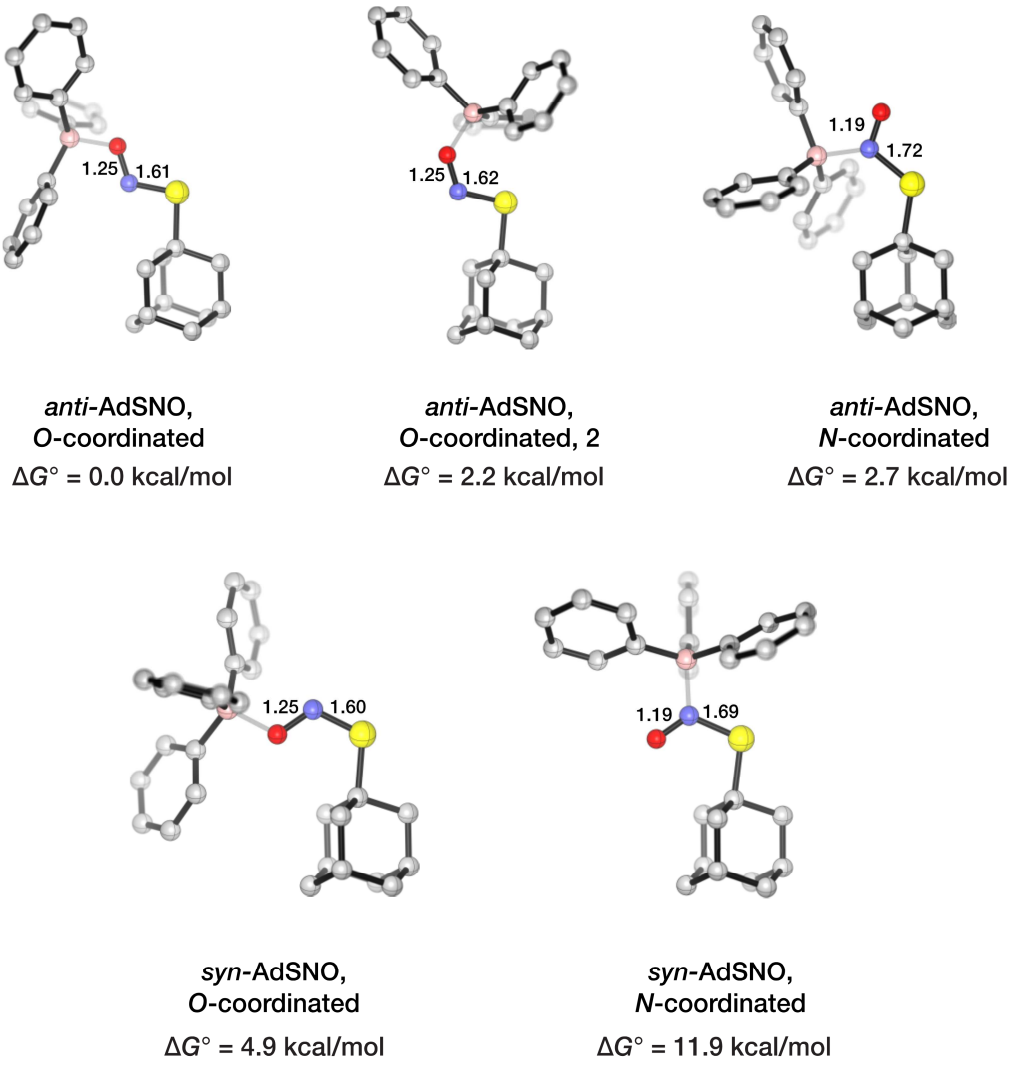

Figure S43. Structures and relative free energies of AdSNO-B(C_6F_5)$_3$ complexes calculated at the ωB97XD-PCM(CH_2Cl_2)/ma-def2-TZVPP level. Bond lengths in Å; hydrogen and fluorine atoms not shown for clarity.

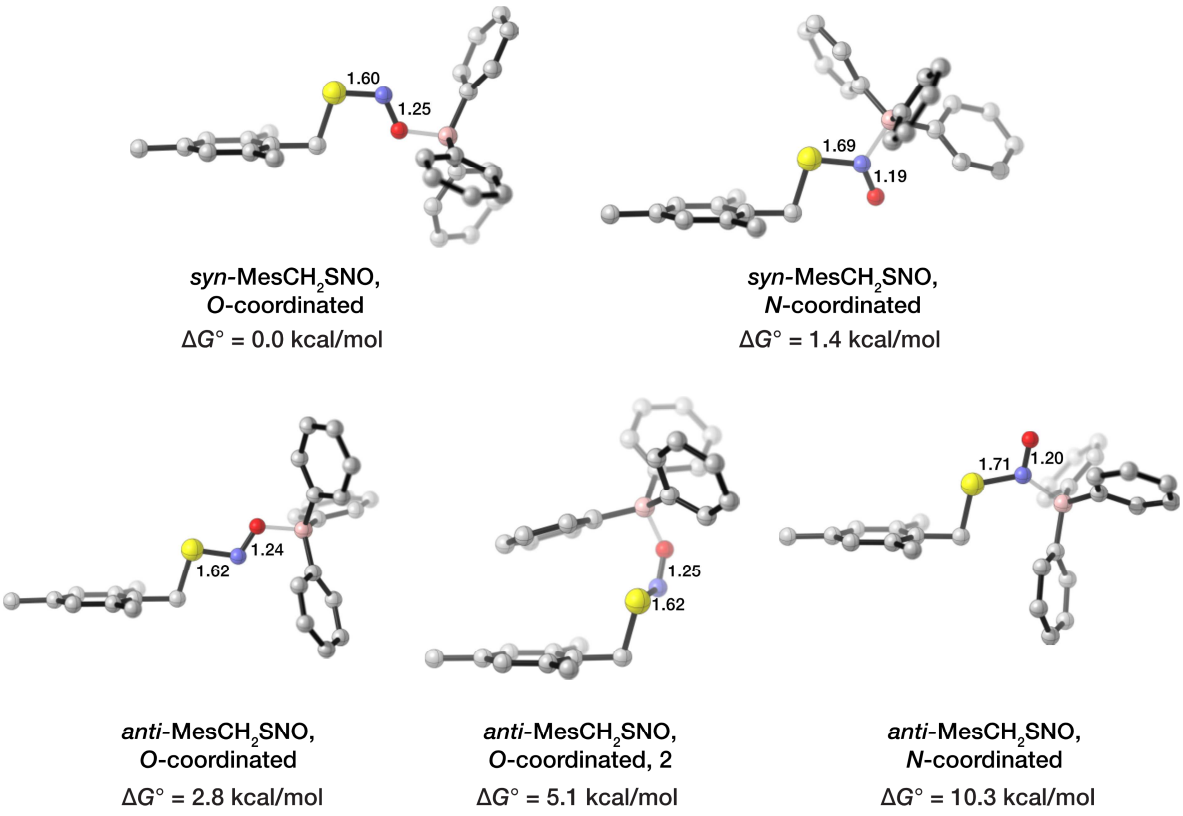

Figure S44. Structures and relative free energies of $MesCH_2SNO\text{-}B(C_6F_5)_3$ complexes calculated at the ωB97XD-PCM(CH_2Cl_2)/ma-def2-TZVPP level. Bond lengths in Å; hydrogen and fluorine atoms not shown for clarity.

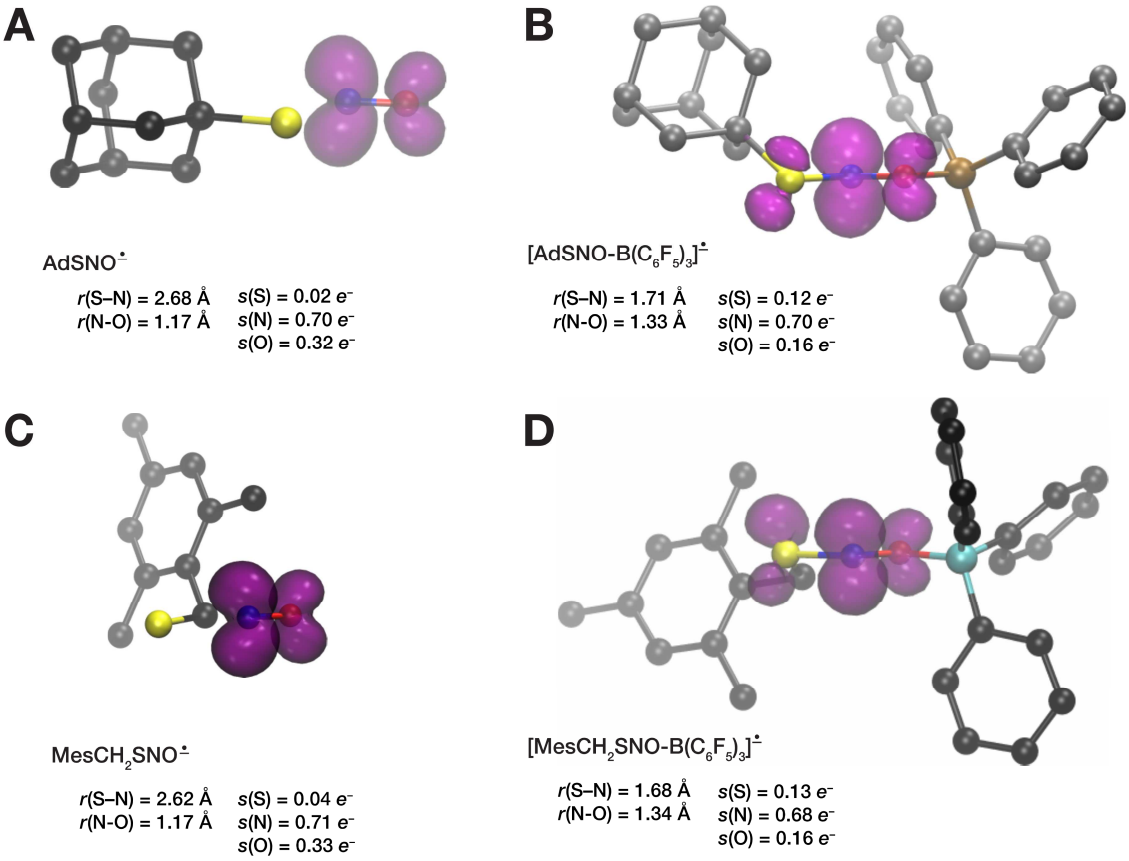

Figure S45. Unpaired spin density distribution (0.004 au isosurfaces) in RSNO anion-radicals (**A**, **C**) and the corresponding RSNO-B(C_6F_5)$_3$ anion-radicals (**B**, **D**) with corresponding S–N and N–O bond lengths and total spin populations ***s*** on the –SNO group atoms calculated at the ωB97XD-PCM(CH_2Cl_2)/ma-def2-TZVPP level. Hydrogen and fluorine atoms not shown for clarity.

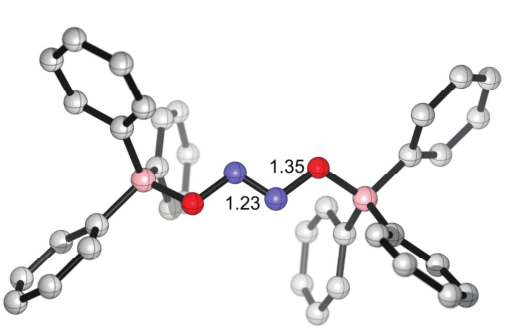

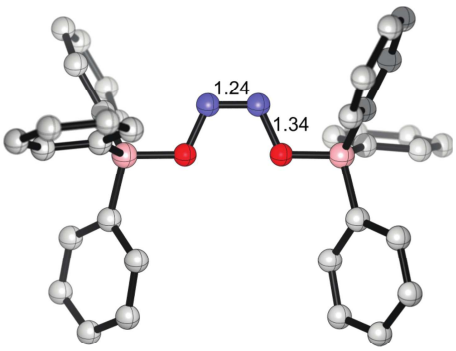

trans-$(C_6F_5)_3BO–N=N–OB(C_6F_5)_3^{2-}$

$\Delta G°$ = 0.0 kcal/mol
$\Delta H°$ = 0.0 kcal/mol

δ ^{15}N 425 ppm

cis-$(C_6F_5)_3BO–N=N–OB(C_6F_5)_3^{2-}$

$\Delta G°$ = +1.6 kcal/mol
$\Delta H°$ = +0.6 kcal/mol

δ ^{15}N 380 ppm

Figure S46. Two forms of $[(C_6F_5)_3BONNOB(C_6F_5)_3]^{2-}$ calculated at the ωB97XD-PCM(CH_2Cl_2)/red-ma-def2-SV(P) level: relevant bond lengths (Å), relative energies, and predicted ^{15}N NMR shifts. Hydrogen and fluorine atoms not shown for clarity.

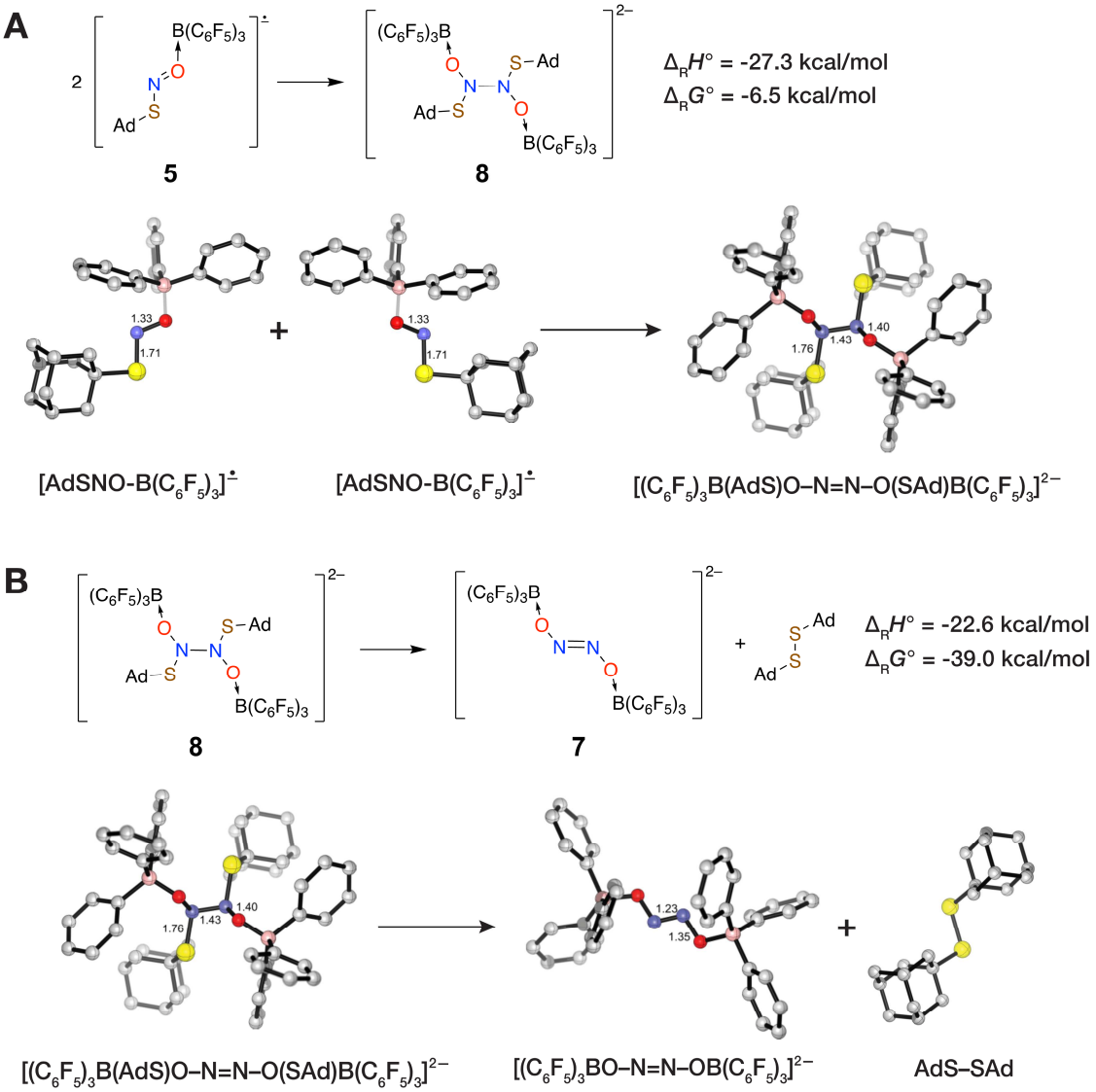

Figure S47. Thermodynamic parameters of (**A**) the dimerization reaction of the AdSNO-$B(C_6F_5)_3$ anion-radical and (**B**) subsequent AdS–SAd elimination calculated at the ωB97XD-PCM(CH_2Cl_2)/red-ma-def2-SV(P) level. Hydrogen and fluorine atoms not shown for clarity.

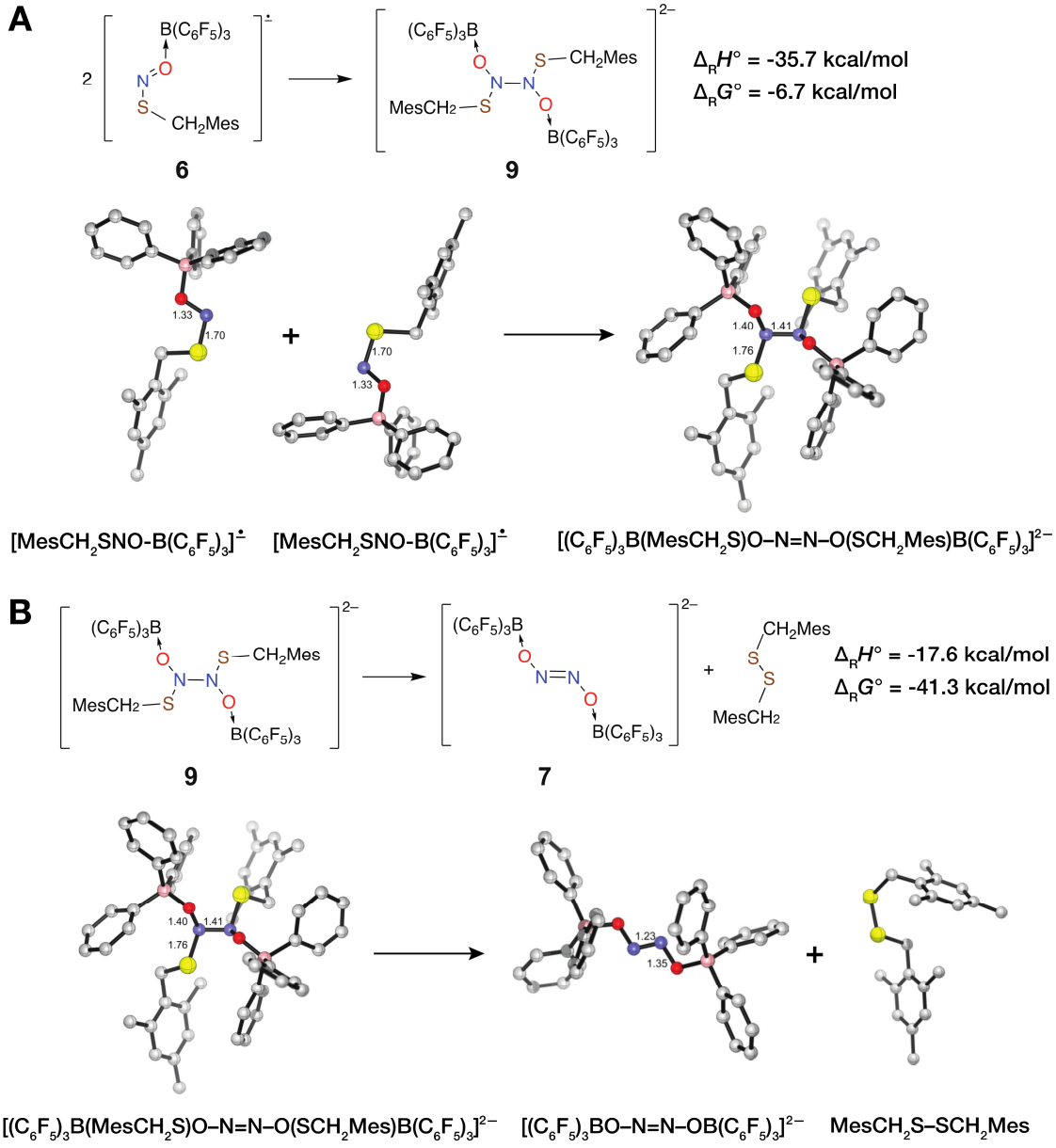

Figure S48 Thermodynamic parameters of (**A**) the dimerization reaction of the $MesCH_2SNO\text{-}B(C_6F_5)_3$ anion-radical and (**B**) subsequent $MesCH_2S–SCH_2Mes$ elimination calculated at the ωB97XD-PCM(CH_2Cl_2)/red-ma-def2-SV(P) level. Hydrogen and fluorine atoms not shown for clarity.

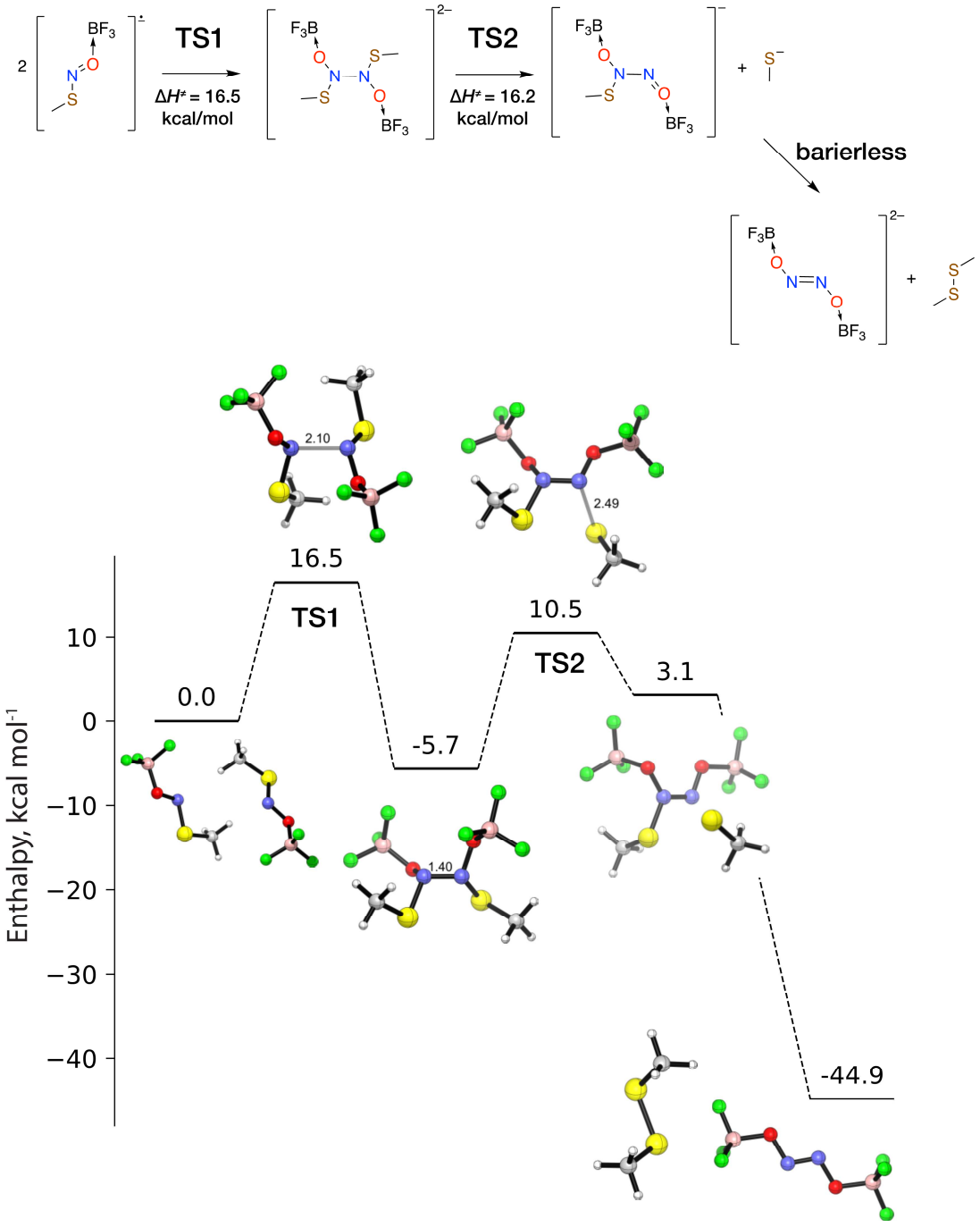

Figure S49. Full reaction profile for the dimerization reaction of the small model system, CH_3SNO-BF_3 anion-radical, and subsequent CH_3S–SCH_3 elimination calculated at the ωB97XD-PCM(CH_2Cl_2)/ma-def2-TZVPP level; broken-symmetry unrestricted calculations have been used for the open-shell TS1 structure ($\langle S^2 \rangle$=0.40); transition structures have been verified with IRC calculations. Bond lengths in Å.

17. References

(1) Girard, P.; Guillot, N.; Motherwell, W. B.; Hay-Motherwell, R. S.; Potier, P. The reaction of thionitrites with barton esters: a convenient free radical chain reaction for decarboxylative nitrosation, *Tetrahedron,* **1999**, *55,* 3573-3584.

(2) Melzer, M. M.; Mossin, S.; Cardenas, A. J.; Williams, K. D.; Zhang, S.; Meyer, K.; Warren, T. H. A Copper(II) Thiolate from Reductive Cleavage of an S-Nitrosothiol *Inorg. Chem.* **2012**, *51*, 8658–8660.

(3) Kundu, S.; Kim, W. Y.; Bertke, J. A.; Warren, T. H. Copper(II) Activation of Nitrite: Nitrosation of Nucleophiles and Generation of NO by Thiols, *J. Am. Chem. Soc.* **2017**, *139,* 1045-1048.

(4) Chai, J.-D.; Head-Gordon, M., Long-range corrected hybrid density functionals with damped atom–atom dispersion corrections. *Physical Chemistry Chemical Physics* **2008,** *10* (44), 6615-6620.

(5) Khomyakov, D. G.; Timerghazin, Q. K., Toward reliable modeling of S-nitrosothiol chemistry: Structure and properties of methyl thionitrite (CH3SNO), an S-nitrosocysteine model. *The Journal of chemical physics* **2017,** *147* (4), 044305.

(6) Weigend, F.; Ahlrichs, R., Balanced basis sets of split valence, triple zeta valence and quadruple zeta valence quality for H to Rn: Design and assessment of accuracy. *Physical Chemistry Chemical Physics* **2005,** *7* (18), 3297-3305.

(7) Zheng, J.; Xu, X.; Truhlar, D. G., Minimally augmented Karlsruhe basis sets. *Theoretical Chemistry Accounts* **2011,** *128* (3), 295-305.

(8) Frisch, M. J.; Trucks, G. W.; Schlegel, H. B.; Scuseria, G. E.; Robb, M. A.; Cheeseman, J. R.; Scalmani, G.; Barone, V.; Petersson, G. A.; Nakatsuji, H.; Li, X.; Caricato, M.; Marenich, A. V.; Bloino, J.; Janesko, B. G.; Gomperts, R.; Mennucci, B.; Hratchian, H. P.; Ortiz, J. V.; Izmaylov, A. F.; Sonnenberg, J. L.; Williams; Ding, F.; Lipparini, F.; Egidi, F.; Goings, J.; Peng, B.; Petrone, A.; Henderson, T.; Ranasinghe, D.; Zakrzewski, V. G.; Gao, J.; Rega, N.; Zheng, G.; Liang, W.; Hada, M.; Ehara, M.; Toyota, K.; Fukuda, R.; Hasegawa, J.; Ishida, M.; Nakajima, T.; Honda, Y.; Kitao, O.; Nakai, H.; Vreven, T.; Throssell, K.; Montgomery Jr., J. A.; Peralta, J. E.; Ogliaro, F.;

Bearpark, M. J.; Heyd, J. J.; Brothers, E. N.; Kudin, K. N.; Staroverov, V. N.; Keith, T. A.; Kobayashi, R.; Normand, J.; Raghavachari, K.; Rendell, A. P.; Burant, J. C.; Iyengar, S. S.; Tomasi, J.; Cossi, M.; Millam, J. M.; Klene, M.; Adamo, C.; Cammi, R.; Ochterski, J. W.; Martin, R. L.; Morokuma, K.; Farkas, O.; Foresman, J. B.; Fox, D. J. *Gaussian 16 Rev. C.01*, Wallingford, CT, 2016.

(9) Cheeseman, J. R.; Trucks, G. W.; Keith, T. A.; Frisch, M. J., A comparison of models for calculating nuclear magnetic resonance shielding tensors. *The Journal of chemical physics* **1998,** *104* (14), 5497-5509.

(10) Reed, A. E.; Weinstock, R. B.; Weinhold, F., Natural population analysis. *The Journal of chemical physics* **1985,** *83* (2), 735-746.

(11) Glendening, E. D.; Badenhoop, J. K.; Weinhold, F., Natural resonance theory: III. Chemical applications. *Journal of Computational Chemistry* **1998,** *19* (6), 628-646.

(12) Glendening, E. D.; Landis, C. R.; Weinhold, F., Resonance Theory Reboot. *J. Am. Chem. Soc.* **2019,** *141* (10), 4156-4166.

(13) Glendening, E. D.; Landis, C. R.; Weinhold, F., NBO 7.0: New vistas in localized and delocalized chemical bonding theory. *Journal of Computational Chemistry* **2019,** *40* (25), 2234-2241.

(14) Glendening, E. D.; Weinhold, F., Natural resonance theory: II. Natural bond order and valency. *Journal of Computational Chemistry* **1998,** *19* (6), 610-627.

(15) Glendening, E. D.; Weinhold, F., Natural resonance theory: I. General formalism. *Journal of Computational Chemistry* **1998,** *19* (6), 593-609.